ORIGINAL ARTICLE

Vibration and frequency analysis of edge-cracked functionally graded graphene reinforced composite beam with piezoelectric actuators

J. J. Mao[1] · L. J. Guo[1] · W. Zhang[1]

Abstract

This paper investigates vibrations of the edge-cracked functionally graded graphene reinforced composite (FG-GRC) beam with the piezoelectric actuators. The edge crack is simulated by a rotational massless spring model. The effective Young modulus of the FG-GRC beam is estimated by utilizing the modified Halpin–Tsai model. The rule of mixture is applied to calculate the mass density and Poisson ratio of the FG-GRC beam. The total energy function of the edge-cracked FG-GRC piezoelectric beam is derived through using Timoshenko beam theory and von Kármán nonlinear strain–displacement relationship. The mechanical–electrical governing equations of motion for the edge-cracked FG-GRC piezoelectric beam are obtained by applying the standard Ritz procedure and are solved by the direct iterative method. The effectiveness and accuracy of this approach are verified through comparing the present results with other research results. Both uniformly and functionally graded (FG) distributed graphene nanoplatelets (GPLs) are considered to analyze influences of the GPL weight fraction, crack depth, crack location, boundary condition, thickness of the piezoelectric layer, and applied actuator voltage on the mechanical–electrical linear and nonlinear vibrations of the edge-cracked FG-GRC beam. The numerical results can help us predict the mechanical–electrical dynamic behaviors of the FG-GRC beam with cracks and promote the development of the structural health monitoring.

Keywords Graphene reinforced composites · Functionally graded materials · Piezoelectric layers · Vibration · Edge crack

1 Introduction

Since Novoselov et al. [1] reported the novel two-dimensional material, namely, graphene, it has attracted the extensive attentions of scientists and engineers as its excellent mechanical, thermal, electrical properties and low mass density. For example, Young modulus and ultimate strength of the graphene and its derivatives can respectively reach up to 1 TPa and 130 GPa [2], and the limit of the intrinsic mobility is 2×10^5 cm^{2}V^{-1}s^{-1}, which exceeds the known highest materials [3]. The theories and experiments observed that a low filler content of the graphene and its derivatives can introduce a dramatic improvement in the properties of the polymer, ceramic, and metal [4–7]. Rafiee et al. [6] presented an experimental research on the graphene-based epoxy nanocomposites and found that Young modulus of the nanocomposite increases to 31% when 0.1% weight fraction of the GPLs is added. The GPL reinforced composites (GRCs) are promising to be the next age group composites in aerospace, mechanical, and civil engineering fields. During the service of the engineering structures, the crack problems are unavoidable. It is well known that the vibration behaviors have significantly influenced because of the local flexibility introduced by the edge cracks of the structures. The present paper originally investigates the linear and nonlinear vibrations of the edge-cracked functionally graded graphene reinforced composite (FG-GRC) beam with the piezoelectric actuators under the coupled effect of the electric and mechanical fields. This paper aims at the vibrations of the edge-cracked FG-GRC piezoelectric beam. However, our previous article [8] mainly was the analysis on the static

✉ W. Zhang
sandyzhang0@yahoo.com

J. J. Mao
jiajia.mao@bjut.edu.cn

L. J. Guo
guolijia@emails.bjut.edu.cn

[1] Beijing Key Laboratory of Nonlinear Vibrations and Strength of Mechanical Structures, Faculty of Materials and Manufacturing, Beijing University of Technology, Beijing 100124, People's Republic of China

buckling behaviors. The vibration in our present paper is much more complicate than the static problem.

Carrying out the continuous and smooth behaviors, the functionally graded material (FGM) usually consists of two or more distinct component materials whose volume fractions or weight fractions vary continuously. Zhao et al. [5] presented a comprehensive review about researches of the mechanical analyses for the FG-GRC structures. With the help of the FGMs, the mismatches caused by different materials can be effectively alleviated or eliminated [9]. Also, the FGM significantly improves the stability and resistance to the damage of the structures [10–17]. Esen et al. [18] studied the vibration and buckling stability of Timoshenko FG beam under the thermal and magnetic environment. Hamed et al. [19] optimized the critical buckling load of the sandwich beam with the porous core by adjusting the distribution of the carbon nanotubes (CNTs). Daikh et al. [20] gave a comprehensive analysis on the static buckling and static deflection of the CNT reinforced FG composite plate.

Yang's group firstly introduced the FG distributed graphene nanoplatelets (GPLs) into the polymer matrix [21] and illustrated that a little amount of the GPLs can remarkably improve the vibration properties of the FG-GRC beam [22]. Simultaneously, Shen's team used Reedy third-order shear deformation theory to research the linear and nonlinear properties of the FG-GRC structures under the thermal environment [23, 24]. Zhang and his colleagues researched the buckling, postbuckling, and vibrations of the FG graphene reinforced laminated composite structures [25–27]. Wang et al. [28] investigated the vibrations and bending behaviors of the FG-GRC doubly curved shallow shells. Esen et al. [29] presented the size-dependent finite element model to analyze the Timoshenko microbeam. Mohamed et al. [30] proposed an energy-equivalent model to study the size scale effect on the buckling and postbuckling properties of the CNT. Recently, Zhang's group [31] took the small-scale effect into consideration to analyze the dynamic stability of the FG-GRC structures.

All aforementioned works paid attention to the intact FG-GRC structures. In fact, there are few structures working without the defects in engineering [32]. The defects, such as initial bending [33, 34] and crack [35, 36], caused by the manufacture or complex environment during their service, are unavoidable in engineering applications. The defects can significantly reduce the local stiffness and strength, hence notably affect the behaviors of the structures [37, 38]. Understanding the performances of the structures with the defects is one of the key factors for avoiding unexpected structural destruction and guaranteeing their safety operation. Broek [39] gave an oversight of the engineering fracture mechanics. Erdogan and Wu [40] and Guo et al.

[41], respectively, made great contribution to the static and dynamic fracture mechanics of the FGM structures. Their results stated that the behaviors of the FG structure with an edge crack is more complex than that with the internal crack problem [37], especially for the dynamic behaviors. With an equivalent lumped stiffness, the edge-cracked structure can be simulated as two substructures connected by a line spring [42, 43]. Yang and his coauthors [44–47] analyzed the vibrations, buckling, and postbuckling behaviors of the edge-cracked FGM Euler–Bernoulli and Timoshenko beams by utilizing the line spring model. Zhu et al. [43, 48] investigated the vibration and crack identification of the edge-cracked structures. There were also other researchers of reporting the cracked FGM structures. Please refer to the recent reviews [37, 49, 50].

It is worth noticed that the cracked FG-GRC structures seldom received attentions, even more and more FG-GRC structures were applied in engineering fields. Until now, only Song and his co-workers [38, 42, 51] calculated the stress intensity factor (SIF) of the edge-cracked FG-GRC beam and investigated their vibration, buckling, and postbuckling behaviors. Their results revealed that the coupled effect of the GPLs and crack characteristics has significant influence on the performances of the edge-cracked FG-GRC beam. Recently, the smart structures played important roles in the advanced fields as they can actively maintain their optimum conditions in response to the varying environment [52–57]. They were usually fabricated by the structural host covering with the piezoelectric actuators. Consequently, the performances of the smart FG-GRC structures with cracks have the theoretical and practical significance in the application on the non-destructive damage detection of the smart GRCs.

This paper studies the linear and nonlinear vibrations of an edge-cracked FG-GRC beam covered by the piezoelectric actuators. The bending stiffness of the cracked section is evaluated by a rotational massless spring model for the edge-cracked FG-GRC piezoelectric beam. Three different GPL distribution patterns are considered. The modified Halpin–Tsai model and rule of mixture are used to calculate the effective Young modulus and other mechanical properties of the edge-cracked FG-GRC piezoelectric beam. In the framework of von Kármán nonlinear strain–displacement relationship, Timoshenko beam theory, and Ritz method, the mechanical–electrical governing equations of motion are deduced for the edge-cracked FG-GRC piezoelectric beam. The effects of the GPL distribution pattern, GPL weight fraction, crack depth, crack location, boundary condition, thickness of piezoelectric layer, and applied actuator voltage on the vibrations of the edge-cracked FG-GRC piezoelectric beam are parametrically investigated.

2 Theoretical formulation

Figure 1a indicates a multi-layered FG-GRC beam of the length L, width b, and thickness h, containing an edge crack of the depth a at a distance L_1 from the left end. The multi-layered FG-GRC beam is consisted of a mixture of the isotropic polymer matrix and GPLs with length l_G, width w_G, and thickness h_G. It is assumed that the crack is perpendicular to the top surface of the FG-GRC beam and remains open, namely, the mode I crack. The unfaulted part of the cross section with the crack for the FG-GRC beam is simulated by utilizing the rotating spring of the large stiffness. Two sub-beams are connected by a massless rotational spring with the large stiffness. Therefore, the model of the rotational spring is employed to calculate the bending stiffness of the unfaulted part [38], as shown in Fig. 1b. The bending stiffness of the unfaulted part is simulated through using the torsional stiffness of the rotational spring. The torsional stiffness of the rotational spring is derived by

$$K_T = \frac{1}{G}, \tag{1}$$

where G is the flexibility.

According to Broek's approximation [39], G is derived as

$$\frac{1 - v(a)^2}{Y(a)} K_I^2 = \frac{M_I^2}{2} \frac{dG}{da}, \tag{2}$$

and

$$K_I = \frac{6 M_I \sqrt{\pi a}}{h^2} F(a), \tag{3}$$

where M_I denotes the bending moment on the cracked section, K_I represents the SIF under the mode I loading, and $Y(a)$ and $v(a)$, respectively, denote Young modulus and Poisson ratio on the crack tip.

Substituting Eq. (3) into Eq. (2), the flexibility G is derived as

$$G = \frac{72\pi}{h^2} \left[\frac{1 - v(N_C)^2}{Y(N_C)} \int_{\frac{N_C - 1}{N}}^{\zeta} \varsigma F(\varsigma)^2 d\varsigma \right. \\ \left. + \sum_{k=1}^{N_C - 1} \frac{1 - v(k)^2}{Y(k)} \int_{\frac{a_k}{h}}^{\frac{a_{k+1}}{h}} \varsigma F(\varsigma)^2 d\varsigma \right], \tag{4}$$

where $\zeta = a/h$.

Each GRC layer has the equal thickness Δh. The uniform U and two different FG distributed GPLs are considered, as shown in Fig. 1c. For the FG distribution patterns, namely, FG-O and FG-X types, the GPLs uniformly disperse into each GRC layer, but follow a linearly and symmetrically law along the thickness direction in the FG-GRC beam. The darker color denotes the higher GPL weight fraction. The surfaces of the FG-X and FG-O patterns have the highest and lowest GPL weight fractions, respectively. The main
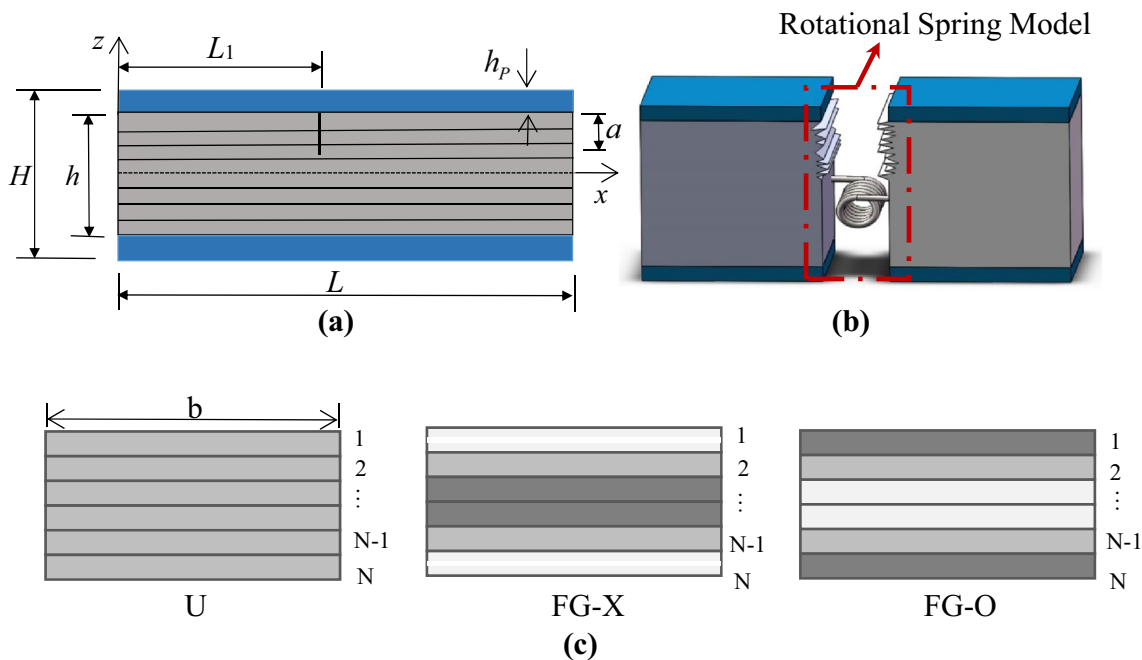

Fig. 1 Schematic map of structural host covering with piezoelectric actuators: **a** a model of an N-layered GRC piezoelectric beam, **b** GPL distribution types: U, FG-X, and FG-O, and **c** rotational spring model

purpose in this paper is to explore the effects of the cracks and graphene reinforcements on the vibrations of the FG-GRC piezoelectric beams. Therefore, we only considered the simple symmetrical distribution of the GPLs. The asymmetric distribution forms of the GPLs is not discussed in this paper and the most of the public references.

There are two piezoelectric actuator layers of the thickness h_P, respectively, bonded on the top and bottom surfaces of the FG-GRC beam. The total thickness of the edge-cracked FG-GRC piezoelectric beam is H. For the FG-GRC beam in an open edge crack, the expression of the SIF is derived by introducing the normalized SIF $F(a)$ which is proposed by Song et al. [38]

The tip of the crack is located in the N_C-th GRC layer. Assuming the total GPL weight fractions for three different patterns have the same value f_G, the GPL volume fraction $V_G^{(k)}$ of the kth ($k = 1, 2, \ldots, N$) layer for the FG-GRC beam with three different GPL distributions are, respectively, given as

U

$$V_G^{(k)} = V_G^*, \tag{5}$$

FG-O

$$V_G^{(k)} = 2V_G^*\left(\frac{1 - |2k - N - 1|}{N}\right), \tag{6}$$

FG-X

$$V_G^{(k)} = 2V_G^*\left(\frac{2k - N - 1}{N}\right), \tag{7}$$

where

$$V_G^* = \frac{f_G}{f_G + (\rho_G/\rho_M)(1 - f_G)}, \tag{8}$$

and the total number N of the GRC layers is an even number, ρ_G and ρ_M are, respectively, the mass density values of the GPLs and matrix.

Shokrieh et al. [58] compared the tensile moduli of the graphene reinforced epoxy among Halpin–Tsai model, Mori–Tanaka model, and experimental test. Their results demonstrated that Halpin–Tsai model is more accurate than Mori–Tanaka model to predict the modules and stiffness of the graphene reinforced epoxy composites. Thus, we apply Halpin–Tsai model in this paper to investigate the vibrations of the functionally graded graphene reinforced beam. According to the modified Halpin–Tsai model and the rule

of mixture, Young modulus $Y_C^{(k)}$, Poisson's ratio $\nu_C^{(k)}$, and mass density $\rho_C^{(k)}$ of the FG-GRC beam are evaluated by [38]

$$Y_C^{(k)} = \frac{3\left(1 + 2\xi_{LW}\xi_{WH}\eta_L V_G^{(k)}\right)}{8\left(1 - \eta_L V_G^{(k)}\right)} \times Y_M + \frac{5\left(1 + 2\xi_{WH}\eta_W V_G^{(k)}\right)}{8\left(1 - \eta_W V_G^{(k)}\right)} \times Y_M, \tag{9}$$

$$\rho_C^{(k)} = \rho_G V_G^{(k)} + \rho_M\left(1 - V_G^{(k)}\right), \tag{10}$$

$$\nu_C^{(k)} = \nu_G V_G^{(k)} + \nu_M\left(1 - V_G^{(k)}\right), \tag{11}$$

where

$$\eta_L = \frac{Y_G/Y_M - 1}{Y_G/Y_M + 2\xi_{LW}\xi_{WH}}, \quad \eta_W = \frac{Y_G/Y_M - 1}{Y_G/Y_M + 2\xi_{WH}}, \tag{12}$$

and Y_G and Y_M, respectively, denote Young moduli of the GPLs and matrix, ν_G and ν_M, respectively, represent Poisson ratios of the GPLs and matrix, and ξ_{LW} and ξ_{WH} are the length-to-width ratio and width-to-thickness ratio, respectively [38],

$$\xi_{LW} = \frac{l_G}{w_G}, \quad \xi_{WH} = \frac{w_G}{h_G}. \tag{13}$$

3 Vibration analysis

According to the theory of Timoshenko beam [31], the displacements $\tilde{u}(x, z, t)$ and $\tilde{w}(x, z, t)$ of an arbitrary point for the edge-cracked FG-GRC piezoelectric beam along the x- and z-axes are given by

$$\tilde{u}(x, z, t) = u(x, t) + z\varphi(x, t), \quad \tilde{w}(x, z, t) = w(x, t), \tag{14}$$

where $u(x, t)$ and $w(x, t)$ denote the displacements on the midplane of the beam, $\varphi(x, t)$ represents the rotation of the cross section of the beam, and t is time.

According to von Kármán nonlinear strain–displacement relationship, the strains are derived as

$$\varepsilon_{xx} = \frac{\partial u}{\partial x} + \frac{1}{2}\left(\frac{\partial w}{\partial x}\right)^2 + z\frac{\partial \varphi}{\partial x}, \quad \gamma_{xz} = \frac{\partial w}{\partial x} + \varphi. \tag{15}$$

Applying the linear elastic constitutive laws to each GRC layer, the relationships between the normal stress $\sigma_{xx}^{(k)}$ and shear stress $\tau_{xz}^{(k)}$ for the kth GRC layer are obtained as

$$\sigma_{xx}^{(k)} = Q_{11}^{(k)}\left[\frac{\partial u}{\partial x} + \frac{1}{2}\left(\frac{\partial w}{\partial x}\right)^2 + z\frac{\partial\varphi}{\partial x}\right], \quad \tau_{xz}^{(k)} = Q_{55}^{(k)}\left(\frac{\partial w}{\partial x} + \varphi\right),$$
(16)

where

$$Q_{11}^{(k)} = \frac{Y_C^{(k)}}{1 - \nu_C^{(k)2}}, \quad Q_{55}^{(k)} = \frac{Y_C^{(k)}}{2\left(1 + \nu_C^{(k)}\right)}.$$
(17)

For the piezoelectric actuator layers, the linear piezoelectric elastic constitutive relationships are given as [54]

$$\sigma_{xx}^P = Q_{11}^P\left[\frac{\partial u}{\partial x} + \frac{1}{2}\left(\frac{\partial w}{\partial x}\right)^2 + z\frac{\partial\varphi}{\partial x} - d_{31}E_z\right], \quad \tau_{xz}^P = Q_{55}^P\left(\frac{\partial w}{\partial x} + \varphi\right),$$
(18)

where

$$Q_{11}^P = \frac{Y_P}{1 - \nu_P^2}, \quad Q_{55}^P = \frac{Y_P}{2\left(1 + \nu_P\right)},$$
(19)

Y_P and ν_P, respectively, are Young modulus and Poisson ratio of the piezoelectric layer, and d_{31} is the piezoelectric strain constant.

When the piezoelectric layer is thin enough, the variation of the electric potential is linear across its thickness [52, 55, 59]. The electric field can be assumed as $(0, 0, E_z)$ when the actuator is poled along the z direction. According to Maxwell equation [60], the electric field intensity E_z of the piezoelectric actuator for the given applied actuator voltage V_0 is expressed as [52, 55, 59]

$$E_z = \frac{V_0}{h_P}.$$
(20)

The potential energy P of the edge-cracked FG-GRC piezoelectric beam is expressed as follows:

$$P = \frac{1}{2}\int_0^{L_1}\sum_{k=1}^N\int_{h/2-k\Delta h}^{h/2-(k-1)\Delta h}\left(\sigma_{xx}^{(k)}\varepsilon_{xx} + \tau_{xz}^{(k)}\gamma_{xz}\right)dzdx$$
$$+ \frac{1}{2}\int_{L_1}^L\sum_{k=1}^N\int_{h/2-k\Delta h}^{h/2-(k-1)\Delta h}\left(\sigma_{xx}^{(k)}\varepsilon_{xx} + \tau_{xz}^{(k)}\gamma_{xz}\right)dzdx$$
$$+ \frac{1}{2}\int_0^{L_1}\int_{-H/2}^{-h/2}\left(\sigma_{xx}^P\varepsilon_{xx} + \tau_{xz}^P\gamma_{xz}\right)dzdx$$
$$+ \frac{1}{2}\int_{L_1}^L\int_{-H/2}^{-h/2}\left(\sigma_{xx}^P\varepsilon_{xx} + \tau_{xz}^P\gamma_{xz}\right)dzdx$$
$$+ \frac{1}{2}\int_0^{L_1}\int_{h/2}^{H/2}\left(\sigma_{xx}^P\varepsilon_{xx} + \tau_{xz}^P\gamma_{xz}\right)dzdx$$
$$+ \frac{1}{2}\int_{L_1}^L\int_{h/2}^{H/2}\left(\sigma_{xx}^P\varepsilon_{xx} + \tau_{xz}^P\gamma_{xz}\right)dzdx + \frac{1}{2}K_T[\Delta\varphi]^2,$$
(21)

where $\Delta\varphi = \varphi_2\left(L_1\right) - \varphi_1\left(L_1\right)$.

We define the stiffness components

$$\begin{pmatrix}A_{11}\\B_{11}\\D_{11}\end{pmatrix} = \sum_{k=1}^N\int_{h/2-k\Delta h}^{h/2-(k-1)\Delta h}Q_{11}^{(k)}\begin{pmatrix}1\\z\\z^2\end{pmatrix}dz$$
$$+ \int_{-H/2}^{-h/2}Q_{11}^P\begin{pmatrix}1\\z\\z^2\end{pmatrix}dz + \int_{h/2}^{H/2}Q_{11}^P\begin{pmatrix}1\\z\\z^2\end{pmatrix}dz,$$
(22)

$$A_{55} = \sum_{k=1}^N\int_{h/2-k\Delta h}^{h/2-(k-1)\Delta h}Q_{55}^{(k)}k_s dz + \int_{-H/2}^{-h/2}Q_{55}^P k_s dz + \int_{h/2}^{H/2}Q_{55}^P k_s dz,$$
(23)

where $k_s = 5/6$ is the shear correction factor.

Combining together Eqs. (15)–(19), (22), and (23), the potential energy V of the edge-cracked FG-GRC piezoelectric beam is rewritten as

$$P = \frac{1}{2}\int_0^{L_1}\left\{A_{11}\left[\left(\frac{\partial u_1}{\partial x}\right)^2 + \frac{\partial u_1}{\partial x}\left(\frac{\partial w_1}{\partial x}\right)^2 + \frac{1}{4}\left(\frac{\partial w_1}{\partial x}\right)^4\right] + B_{11}\left[2\frac{\partial u_1}{\partial x}\frac{\partial\varphi_1}{\partial x} + \frac{\partial\varphi_1}{\partial x}\left(\frac{\partial w_1}{\partial x}\right)^2\right]\right.$$
$$\left. + D_{11}\left(\frac{\partial\varphi_1}{\partial x}\right)^2 + A_{55}\left(\varphi_1 + \frac{\partial w_1}{\partial x}\right)^2 - N_P\left[\frac{\partial u_1}{\partial x} + \frac{1}{2}\left(\frac{\partial w_1}{\partial x}\right)^2\right] - M_P\frac{\partial\varphi_1}{\partial x}\right\}dx$$
$$+ \frac{1}{2}\int_{L_1}^L\left\{A_{11}\left[\left(\frac{\partial u_2}{\partial x}\right)^2 + \frac{\partial u_2}{\partial x}\left(\frac{\partial w_2}{\partial x}\right)^2 + \frac{1}{4}\left(\frac{\partial w_2}{\partial x}\right)^4\right] + B_{11}\left[2\frac{\partial u_2}{\partial x}\frac{\partial\varphi_2}{\partial x} + \frac{\partial\varphi_2}{\partial x}\left(\frac{\partial w_2}{\partial x}\right)^2\right]\right.$$
$$\left. + D_{11}\left(\frac{\partial\varphi_2}{\partial x}\right)^2 + A_{55}\left(\varphi_2 + \frac{\partial w_2}{\partial x}\right)^2 - N_P\left[\frac{\partial u_2}{\partial x} + \frac{1}{2}\left(\frac{\partial w_2}{\partial x}\right)^2\right] - M_P\frac{\partial\varphi_2}{\partial x}\right\}dx$$
$$+ \frac{1}{2}K_T\left[\varphi_2\left(L_1\right) - \varphi_1\left(L_1\right)\right]^2,$$
(24)

where the subscript $i = 1, 2$, respectively, represent the left sub-beam and right sub-beam divided by the crack, and the subscript "P" denotes the electric load.

N_P and M_P are defined as

$$\begin{pmatrix} N_P \\ M_P \end{pmatrix} = \int_{-H/2}^{-h/2} Q_{11}^P d_{31} E_z \begin{pmatrix} 1 \\ z \end{pmatrix} dz + \int_{h/2}^{H/2} Q_{11}^P d_{31} E_z \begin{pmatrix} 1 \\ z \end{pmatrix} dz. \tag{25}$$

Obviously, M_P equals to zero because two piezoelectric layers are symmetric along the plane $y = 0$. The ends at $x = 0$ and $x = L$ for the edge-cracked FG-GRC piezoelectric beam are assumed to be no motion along the x direction:

$$0 = [u]_{x=0}^{x=L} = \left(u_{x=L} - u_{x=L_1} \right) + \left(u_{x=L_1} - u_{x=0} \right) = \int_0^{L_1} \frac{\partial u}{\partial x} dx + \int_{L_1}^L \frac{\partial u}{\partial x} dx. \tag{26}$$

Using Eq. (26), the potential energy P expressed in Eq. (24) is further simplified as

$$V = \frac{1}{2} \int_0^{L_1} \left\{ A_{11} \left[\left(\frac{\partial u_1}{\partial x} \right)^2 + \frac{\partial u_1}{\partial x} \left(\frac{\partial w_1}{\partial x} \right)^2 + \frac{1}{4} \left(\frac{\partial w_1}{\partial x} \right)^4 \right] + B_{11} \left[2 \frac{\partial u_1}{\partial x} \frac{\partial \varphi_1}{\partial x} + \frac{\partial \varphi_1}{\partial x} \left(\frac{\partial w_1}{\partial x} \right)^2 \right] \right.$$
$$+ D_{11} \left(\frac{\partial \varphi_1}{\partial x} \right)^2 + A_{55} \left(\varphi_1 + \frac{\partial w_1}{\partial x} \right)^2 - \frac{1}{2} N_P \left(\frac{\partial w_1}{\partial x} \right)^2 \right\} dx + \frac{1}{2} \int_{L_1}^L \left\{ A_{11} \left[\left(\frac{\partial u_2}{\partial x} \right)^2 + \frac{\partial u_2}{\partial x} \left(\frac{\partial w_2}{\partial x} \right)^2 \right. \right.$$
$$\left. + \frac{1}{4} \left(\frac{\partial w_2}{\partial x} \right)^4 \right] + B_{11} \left[2 \frac{\partial u_2}{\partial x} \frac{\partial \varphi_2}{\partial x} + \frac{\partial \varphi_2}{\partial x} \left(\frac{\partial w_2}{\partial x} \right)^2 \right] + D_{11} \left(\frac{\partial \varphi_2}{\partial x} \right)^2 + A_{55} \left(\varphi_2 + \frac{\partial w_2}{\partial x} \right)^2$$
$$- \frac{1}{2} N_P \left(\frac{\partial w_2}{\partial x} \right)^2 \right\} dx + \frac{1}{2} K_T \left[\varphi_2(L_1) - \varphi_1(L_1) \right]. \tag{27}$$

Letting P_L and P_{NL}, respectively, denote the linear and nonlinear strain energy components, the maximum potential energy P_{max} of the edge-cracked FG-GRC piezoelectric beam under the harmonic motion is given as

$$P_{max} = P_L + P_{NL}, \tag{28}$$

where

$$P_L = \frac{1}{2} \int_0^{L_1} \left\{ A_{11} \left(\frac{\partial u_1}{\partial x} \right)^2 + 2 B_{11} \frac{\partial u_1}{\partial x} \frac{\partial \varphi_1}{\partial x} + D_{11} \left(\frac{\partial \varphi_1}{\partial x} \right)^2 + A_{55} \left(\varphi_1 + \frac{\partial w_1}{\partial x} \right)^2 - \frac{1}{2} N_P \left(\frac{\partial w_1}{\partial x} \right)^2 \right\} dx$$
$$+ \frac{1}{2} \int_{L_1}^L \left\{ A_{11} \left(\frac{\partial u_2}{\partial x} \right)^2 + 2 B_{11} \frac{\partial u_2}{\partial x} \frac{\partial \varphi_2}{\partial x} + D_{11} \left(\frac{\partial \varphi_2}{\partial x} \right)^2 + A_{55} \left(\varphi_2 + \frac{\partial w_2}{\partial x} \right)^2 - \frac{1}{2} N_P \left(\frac{\partial w_2}{\partial x} \right)^2 \right\} dx$$
$$+ \frac{1}{2} K_T \left[\varphi_2(L_1) - \varphi_1(L_1) \right]^2, \tag{29}$$

$$P_{NL} = \frac{1}{2} \int_0^{L_1} \left\{ A_{11} \left[\frac{\partial u_1}{\partial x} \left(\frac{\partial w_1}{\partial x} \right)^2 + \frac{1}{4} \left(\frac{\partial w_1}{\partial x} \right)^4 \right] \right.$$
$$\left. + B_{11} \frac{\partial \varphi_1}{\partial x} \left(\frac{\partial w_1}{\partial x} \right)^2 \right\} dx$$
$$+ \frac{1}{2} \int_{L_1}^L \left\{ A_{11} \left[\frac{\partial u_2}{\partial x} \left(\frac{\partial w_2}{\partial x} \right)^2 + \frac{1}{4} \left(\frac{\partial w_2}{\partial x} \right)^4 \right] \right.$$
$$\left. + B_{11} \frac{\partial \varphi_2}{\partial x} \left(\frac{\partial w_2}{\partial x} \right)^2 \right\} dx. \tag{30}$$

The kinetic energy T of the edge-cracked FG-GRC piezoelectric beam is expressed by

$$T = \frac{1}{2} \int_0^{L_1} \sum_{k=1}^{N} \int_{\frac{h}{2}-k\Delta h}^{\frac{h}{2}-(k-1)\Delta h} \rho_C^{(k)} \left[\left(\frac{\partial u_1}{\partial t} + z\frac{\partial \varphi_1}{\partial t} \right)^2 + \left(\frac{\partial w_1}{\partial t} \right)^2 \right] dz dx$$

$$+ \frac{1}{2} \int_{L_1}^{L} \sum_{k=1}^{N} \int_{\frac{h}{2}-k\Delta h}^{\frac{h}{2}-(k-1)\Delta h} \rho_C^{(k)} \left[\left(\frac{\partial u_2}{\partial t} + z\frac{\partial \varphi_2}{\partial t} \right)^2 + \left(\frac{\partial w_2}{\partial t} \right)^2 \right] dz dx$$

$$+ \frac{1}{2} \int_0^{L_1} \int_{h/2}^{H/2} \rho_P \left[\left(\frac{\partial u_1}{\partial t} + z\frac{\partial \varphi_1}{\partial t} \right)^2 + \left(\frac{\partial w_1}{\partial t} \right)^2 \right] dz dx$$

$$+ \frac{1}{2} \int_{L_1}^{L} \int_{h/2}^{H/2} \rho_P \left[\left(\frac{\partial u_2}{\partial t} + z\frac{\partial \varphi_2}{\partial t} \right)^2 + \left(\frac{\partial w_2}{\partial t} \right)^2 \right] dz dx$$

$$+ \frac{1}{2} \int_0^{L_1} \int_{-H/2}^{-h/2} \rho_P \left[\left(\frac{\partial u_1}{\partial t} + z\frac{\partial \varphi_1}{\partial t} \right)^2 + \left(\frac{\partial w_1}{\partial t} \right)^2 \right] dz dx$$

$$+ \frac{1}{2} \int_{L_1}^{L} \int_{-H/2}^{h/2} \rho_P \left[\left(\frac{\partial u_2}{\partial t} + z\frac{\partial \varphi_2}{\partial t} \right)^2 + \left(\frac{\partial w_2}{\partial t} \right)^2 \right] dz dx, \tag{31}$$

which is further written as

$$T = \frac{1}{2} \int_0^{L_1} \left\{ I_1 \left[\left(\frac{\partial u_1}{\partial t} \right)^2 + \left(\frac{\partial w_1}{\partial t} \right)^2 \right] \right.$$
$$\left. + 2I_2 \left(\frac{\partial u_1}{\partial t} \right) \left(\frac{\partial \varphi_1}{\partial t} \right) + I_3 \left(\frac{\partial \varphi_1}{\partial t} \right)^2 \right\} dx$$
$$+ \frac{1}{2} \int_{L_1}^{L} \left\{ I_1 \left[\left(\frac{\partial u_2}{\partial t} \right)^2 + \left(\frac{\partial w_2}{\partial t} \right)^2 \right] \right.$$
$$\left. + 2I_2 \left(\frac{\partial u_2}{\partial t} \right) \left(\frac{\partial \varphi_2}{\partial t} \right) + I_3 \left(\frac{\partial \varphi_2}{\partial t} \right)^2 \right\} dx. \tag{32}$$

The inertial components I_j ($j = 1, 2$ and 3) are defined as

$$\begin{pmatrix} I_1 \\ I_2 \\ I_3 \end{pmatrix} = \sum_{k=1}^{N} \int_{h/2-k\Delta h}^{h/2-(k-1)\Delta h} \rho_C^{(k)} \begin{pmatrix} 1 \\ z \\ z^2 \end{pmatrix} dz$$
$$+ \int_{-H/2}^{-h/2} \rho^P \begin{pmatrix} 1 \\ z \\ z^2 \end{pmatrix} dz + \int_{h/2}^{H/2} \rho^P \begin{pmatrix} 1 \\ z \\ z^2 \end{pmatrix} dz. \tag{33}$$

Thus, the maximum kinetic energy $T_{\max}$ of the edge-cracked FG-GRC beam under the harmonic motion is given as

$$T_{\max} = \frac{\Omega^2}{2} \int_0^{L_1} \left(I_1 u_1^2 + I_1 w_1^2 + 2I_2 u_1 \varphi_1 + I_3 \varphi_1^2 \right) dx$$
$$+ \frac{\Omega^2}{2} \int_0^{L_1} \left(I_1 u_2^2 + I_1 w_2^2 + 2I_2 u_2 \varphi_2 + I_3 \varphi_2^2 \right) dx, \tag{34}$$

where Ω is the frequency of the nonlinear vibration for the edge-cracked FG-GRC piezoelectric beam.

Introducing the following dimensionless variables and parameters, we have

$$X = \frac{x}{L}, \ X_0 = \frac{L_1}{L}, \ (U, W) = \frac{(u, w)}{H}, \ \psi = \varphi,$$
$$(\tilde{I}_1, \tilde{I}_2, \tilde{I}_3) = \left(\frac{I_1}{I_{10}}, \frac{I_2}{I_{10}H}, \frac{I_3}{I_{10}H^2} \right), \eta = \frac{L}{H},$$
$$(a_{11}, a_{55}, b_{11}, d_{11}) = \left(\frac{A_{11}}{A_{110}}, \frac{A_{55}}{A_{110}}, \frac{B_{11}}{A_{110}H}, \frac{D_{11}}{A_{110}H^2} \right),$$
$$\tilde{N}^P = \frac{N^P}{A_{110}}, \ \omega = \Omega L \sqrt{\frac{I_{10}}{A_{110}}},$$
$$P_L^* = \frac{V_L}{A_{110}H^2/L}, \ P_{\text{NL}}^* = \frac{V_{\text{NL}}}{A_{110}H^2/L},$$
$$T_{\max}^* = \frac{T_{\max}}{A_{110}H^2/L}, \ K_T^* = \frac{K_T}{A_{110}H^2/L}, \tag{35}$$

where A_{110} and I_{10}, respectively, represent the values of A_{11} and I_1 for the homogeneous polymer beam without the edge crack and piezoelectric layers.

Equations (29), (30), and (34) are, respectively, expressed in the dimensionless forms:

$$V_L^* = \frac{1}{2} \int_0^{X_0} \left[a_{11} \left(\frac{\partial U_1}{\partial X} \right)^2 + 2b_{11} \frac{\partial U_1}{\partial X} \frac{\partial \psi_1}{\partial X} + d_{11} \left(\frac{\partial \psi_1}{\partial X} \right)^2 + a_{55} \left(\eta\psi_1 + \frac{\partial W_1}{\partial X} \right)^2 \right.$$
$$\left. - \frac{1}{2}\tilde{N}^P \left(\frac{\partial W_1}{\partial X} \right)^2 \right] dX + \frac{1}{2} \int_{X_0}^{1} \left[a_{11} \left(\frac{\partial U_2}{\partial X} \right)^2 + 2b_{11} \frac{\partial U_2}{\partial X} \frac{\partial \psi_2}{\partial X} + d_{11} \left(\frac{\partial \psi_2}{\partial X} \right)^2 \right.$$
$$\left. + a_{55} \left(\eta\psi_2 + \frac{\partial W_2}{\partial X} \right)^2 - \frac{1}{2}\tilde{N}^P \left(\frac{\partial W_2}{\partial X} \right)^2 \right] dX - \frac{1}{2}K_T^*(\Delta\psi)_{X=X_0}^2, \tag{36}$$

$$V_{\text{NL}}^* = \frac{1}{2} \int_0^{X_0} \left[\frac{a_{11}}{\eta} \frac{\partial U_1}{\partial X} \left(\frac{\partial W_1}{\partial X} \right)^2 + \frac{a_{11}}{4\eta^2} \left(\frac{\partial W_1}{\partial X} \right)^4 + \frac{b_{11}}{\eta} \frac{\partial \psi_1}{\partial X} \left(\frac{\partial W_1}{\partial X} \right)^2 \right] dX$$
$$+ \frac{1}{2} \int_{X_0}^1 \left[\frac{a_{11}}{\eta} \frac{\partial U_2}{\partial X} \left(\frac{\partial W_2}{\partial X} \right)^2 + \frac{a_{11}}{4\eta^2} \left(\frac{\partial W_2}{\partial X} \right)^4 + \frac{b_{11}}{\eta} \frac{\partial \psi_2}{\partial X} \left(\frac{\partial W_2}{\partial X} \right)^2 \right] dX, \tag{37}$$

$$T_{\max}^* = \frac{\omega^2}{2} \int_0^{X_0} \left(\tilde{I}_1 U_1^2 + \tilde{I}_1 W_1^2 + 2\tilde{I}_2 U_1 \psi_1 + \tilde{I}_3 \psi_1^2 \right) dX$$
$$+ \frac{\omega^2}{2} \int_{X_0}^1 \left(\tilde{I}_1 U_2^2 + \tilde{I}_1 W_2^2 + 2\tilde{I}_2 U_2 \psi_2 + \tilde{I}_3 \psi_2^2 \right) dX. \tag{38}$$

Therefore, the total energy of the edge-cracked FG-GRC piezoelectric beam is written as follows:

$$\prod = P_L^* + P_{\text{NL}}^* - T_{\max}^*. \tag{39}$$

The edge-cracked FG-GRC piezoelectric beams under three different boundary conditions are investigated, namely, clamped at both ends (C–C), clamped at the left end and hinged at the right end (C–H), and hinged at both ends (H–H). The edge-cracked FG-GRC piezoelectric beams under three different boundary conditions all have no motion along the x direction. In this work, we are mainly focusing on the dynamic effects of the cracks and graphene reinforcements for the FG-GRC piezoelectric beams with the simply supported and clamped boundary conditions. The free boundary is not considered.

Ritz method [45] is applied to derive the eigenvalue equation of the edge-cracked FG-GRC piezoelectric beam. For the left and right sub-beams, the dimensionless trial functions of Ritz method are supposed as [45]

$$U_1(X) = \sum_{j=1}^n A_j X^j, \ U_2(X) = \sum_{j=1}^n \tilde{A}_j X^{j-1}(1-X), \tag{40}$$

$$W_1(X) = \sum_{j=1}^n B_j X^j, \ W_2(X) = \sum_{j=1}^n \tilde{B}_j X^{j-1}(1-X), \tag{41}$$

and for hinged end

$$\Psi_1(X) = \sum_{j=1}^n C_j X^{j-1}, \ \Psi_2(X) = \sum_{j=1}^n \tilde{C}_j X^{j-1}, \tag{42}$$

for clamped end

$$\Psi_1(X) = \sum_{j=1}^n C_j X^j, \ \Psi_2(X) = \sum_{j=1}^n \tilde{C}_j X^{(j-1)}(1-X), \tag{43}$$

Table 1 The material properties of epoxy, graphene, and PVDF

Material properties	Epoxy [38]	Graphene [38]	PVDF [53]
Young modulus (GPa)	3.0	1010	2.1
Density (kg/m³)	1200	1060	1800
Poisson ratio	0.34	0.186	0.29
Piezoelectric strain constant d_{31} (m/V)	–	–	23×10^{-12}

Table 3 Convergent results: linear fundamental frequencies of the cracked FG-GRC piezoelectric beam polynomial terms n

n	C–C	C–H	H–H
2	0.9682	0.5993	0.3854
3	0.8207	0.5847	0.3669
4	0.8179	0.5795	0.3660
5	0.8179	0.5795	0.3660
6	0.8179	0.5795	0.3660
7	0.8179	0.5795	0.3660

Table 2 The convergent results for the linear and nonlinear fundamental frequencies of a cracked FG-X GRC piezoelectric beam with different total number N of the GRC layers

N	C–C		C–H		H–H	
	ω_L	ω_{NL} $w_{\max}/H = 0.5$	ω_L	ω_{NL} $w_{\max}/H = 0.5$	ω_L	ω_{NL} $w_{\max}/H = 0.5$
4	0.7999	0.8739	0.5661	0.6885	0.3567	0.4926
6	0.8124	0.8852	0.5754	0.6960	0.3633	0.4974
8	0.8147	0.8874	0.5771	0.6975	0.3640	0.4979
10	0.8179	0.8902	0.5795	0.6994	0.3660	0.4993
11	0.8170	0.8891	0.5789	0.6984	0.3653	0.4983
12	0.8176	0.8901	0.5793	0.6993	0.3655	0.4990
13	0.8182	0.8904	0.5798	0.6993	0.3660	0.4990

Table 4 Comparison results: dimensionless nonlinear vibration fundamental frequency of the GPL/epoxy composite beam

Boundary	U	FG-O	FG-X
C–C			
Feng et al. [21]	0.58302	0.50870	0.65875
Present	0.56822	0.49062	0.63495
C–H			
Feng et al. [21]	0.43263	0.39101	0.49152
Present	0.44933	0.40171	0.49156

Table 5 Comparison results: linear fundamental frequency ratios of the edge-cracked FG-GRC beam with different crack locations

GPLs distribution	L_1/L				
	0.1	0.2	0.3	0.4	0.5
U					
Song et al. [38]	0.9638	0.9986	0.9889	0.9607	0.9474
Present	0.9610	0.9987	0.9876	0.9564	0.9417
FG-O					
Song et al. [38]	0.9705	0.9989	0.9913	0.9690	0.9584
Present	0.9586	0.9986	0.9869	0.9534	0.9378
FG-X					
Song et al. [38]	0.9557	0.9983	0.9857	0.9498	0.9332
Present	0.9578	0.9985	0.9864	0.9522	0.9363

Table 6 Comparison results: nonlinear to linear fundamental frequency ratios of piezoelectric CNTRC beams

SWCNTs distribution	W_{max}/H		
	0.5	1.0	1.5
U			
Rafiee et al. [52]	1.0056	1.0223	1.0499
Present	1.0066	1.0265	1.0590
FG-O			
Rafiee et al. [52]	1.0085	1.0337	1.0754
Present	1.0103	1.0405	1.0885
FG-X			
Rafiee et al. [52]	1.0042	1.0167	1.0373
Present	1.0050	1.0199	1.0444

where n is the total number of the polynomial terms, and the unknown coefficients A_j, $\tilde{A}_j$, B_j, $\tilde{B}_j$, C_j, and $\tilde{C}_j$ are determined by the boundaries of the edge-cracked FG-GRC piezoelectric beam.

Because of the continuity of the edge-cracked FG-GRC piezoelectric beam, the axial displacements and transverse deflections of the left and right sub-beams at the edge-cracked section satisfy the compatibility conditions:
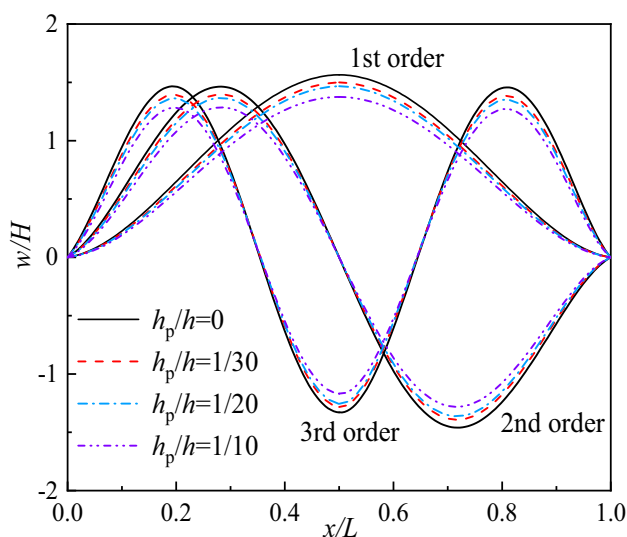

Fig. 2 Effect of the thickness of the piezoelectric layer on the first three linear mode shapes for the edge-cracked C–C X-GRC piezoelectric beam is plotted

$$U_1(X_0) = U_2(X_0), \ W_1(X_0) = W_2(X_0). \tag{44}$$

However, a jumping exists because the bending leads to their rotations

$$\psi_2(X_0) - \psi_1(X_0) = \frac{1}{K_T^*}\left(b_{11}\frac{\partial U_2}{\partial X} + d_{11}\frac{\partial \Psi_2}{\partial X}\right)_{X=X_0}. \tag{45}$$

For the convenient calculation, the nonlinear terms on the right side of the trial functions (45) are ignored to obtain the approximately value of the bending stiffness at the crack section [44]. It is pointed out that the trial functions given by Eqs. (40)–(43) must be modified, because they do not satisfy the conditions of the compatibility in Eqs. (44) and (45). We keep unchanged for the trial functions of the right sub-beam, but modified those of the left sub-beam for the edge-cracked FG-GRC piezoelectric beam [45],

$$U_1(X) = U_a(X) + U_b(X), \ W_1(X) = W_a(X) + W_b(X), \tag{46}$$

$$\psi_1(X) = \psi_a(X) + \psi_b(X) + \psi_c(X), \tag{47}$$

where

$$U_a(X) = \sum_{j=1}^{n} A_j X^j (X - X_0), \ U_b(X) = \frac{X}{X_0}\sum_{j=1}^{n} \tilde{A}_j X_0^{(j-1)}(1 - X_0), \tag{48}$$

$$W_a(X) = \sum_{j=1}^{n} B_j X^j (X - X_0), \ W_b(X) = \frac{X}{X_0}\sum_{j=1}^{n} \tilde{B}_j X_0^{(j-1)}(1 - X_0), \tag{49}$$

and for H–H beam

$$\psi_a(X) = \sum_{j=1}^{n} C_j X^{j-1}\left(X - X_0\right), \quad \psi_b(X) = \sum_{j=1}^{n} \tilde{C}_j\left[X^{j-1} - \frac{d_{11}}{K_T^*}(j-1)X_0^{j-2}\right],$$

$$\psi_c(X) = -\frac{b_{11}}{K_T^*}\sum_{j=1}^{n} \tilde{A}_j\left[(j-1)X_0^{j-2}\left(1 - X_0\right) - X_0^{j-1}\right], \tag{50}$$

for C–H beam

$$\psi_a(X) = \sum_{j=1}^{n} C_j X^{j}\left(X - X_0\right), \quad \psi_b(X) = \frac{X}{X_0}\left[\sum_{j=1}^{n} \tilde{C}_j X_0^{j-1} - \frac{d_{11}}{K_T^*}\sum_{j=1}^{n}\tilde{C}_j(j-1)X_0^{j-2}\right],$$

$$\psi_c(X) = -\frac{X}{X_0}\frac{b_{11}}{K_T^*}\sum_{j=1}^{n} \tilde{A}_j\left[(j-1)X_0^{j-2}\left(1 - X_0\right) - X_0^{j-1}\right], \tag{51}$$

for C–C beam

$$\psi_a(X) = \sum_{j=1}^{n} C_j X^{j}\left(X - X_0\right), \quad \psi_b(X) = \frac{X}{X_0}\sum_{j=1}^{n} \tilde{C}_j\left\{X_0^{j-1}\left(1 - X_0\right) - \frac{d_{11}}{K_T^*}\left[(j-1)X_0^{j-2}\left(1 - X_0\right) - X_0^{j-1}\right]\right\},$$

$$\psi_c(X) = -\frac{X}{X_0}\frac{b_{11}}{K_T^*}\sum_{j=1}^{n} \tilde{A}_j\left[(j-1)X_0^{j-2}\left(1 - X_0\right) - X_0^{j-1}\right]. \tag{52}$$

Substituting Eqs. (46)–(52) into the energy function (39) and employing Ritz procedure [45] to minimize the total energy with respect to the unknown coefficients, we obtain

$$\frac{\partial \Pi}{\partial A_j} = 0, \quad \frac{\partial \Pi}{\partial \tilde{A}_j} = 0, \quad \frac{\partial \Pi}{\partial B_j} = 0, \quad \frac{\partial \Pi}{\partial \tilde{B}_j} = 0, \quad \frac{\partial \Pi}{\partial C_j} = 0, \quad \frac{\partial \Pi}{\partial \tilde{C}_j} = 0. \tag{53}$$

The nonlinear eigenvalue equations of the edge-cracked FG-GRC piezoelectric beam are obtained as

$$\left(\mathbf{K_L} + \frac{1}{2}\mathbf{K_{NL1}} + \frac{1}{3}\mathbf{K_{NL2}}\right)\mathbf{d} - \omega^2 \mathbf{M}\mathbf{d} = 0, \tag{54}$$

where $\mathbf{d} = \left\{\{A_j\}^{\mathrm{T}}, \{\tilde{A}_j\}^{\mathrm{T}}, \{B_j\}^{\mathrm{T}}, \{\tilde{B}_j\}^{\mathrm{T}}, \{C_j\}^{\mathrm{T}}, \{\tilde{C}_j\}^{\mathrm{T}}\right\}^{\mathrm{T}}$, $j = 1 \cdots n$; the mass matrix $\mathbf{M}$, linear stiffness matrix $\mathbf{K_L}$, and nonlinear stiffness matrices $\mathbf{K_{NL1}}$ and $\mathbf{K_{NL2}}$ are all $6n \times 6n$ symmetric matrices.
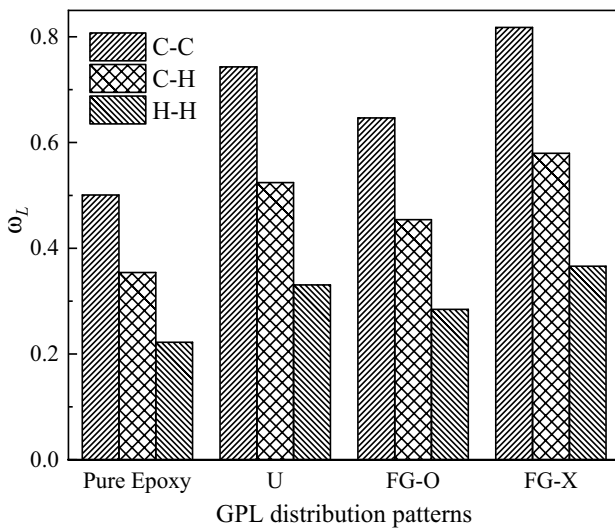

Fig. 3 Effects of the boundary conditions and GPL distributions on the linear fundamental frequencies of the edge-cracked FG-GRC piezoelectric beam
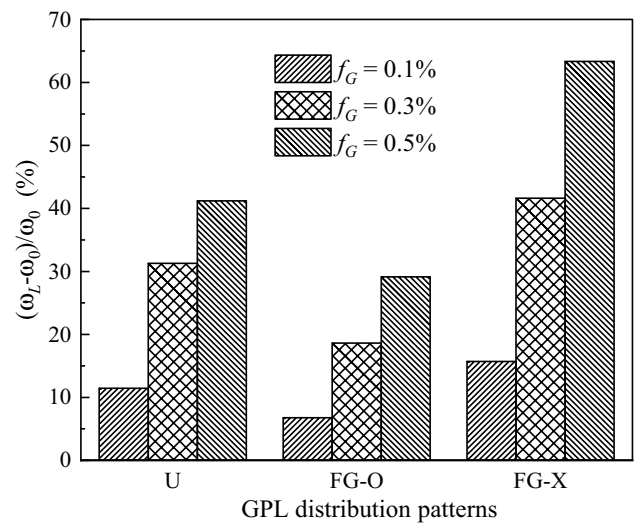

Fig. 4 Effect of the GPL distribution patterns on the linear fundamental frequency change ratios of the edge-cracked C–C GRC piezoelectric beam with varying GPL weight fractions
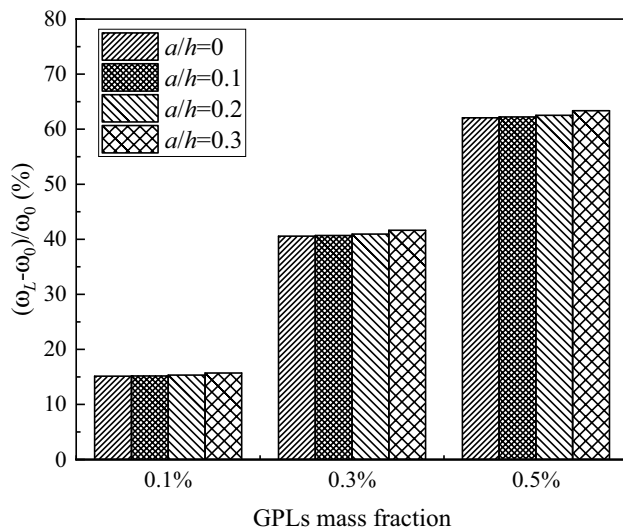
Fig. 5 Effect of the GPL weight fraction on the linear fundamental frequency change ratio of the C–C X-GRC piezoelectric beam with different edge-crack depths
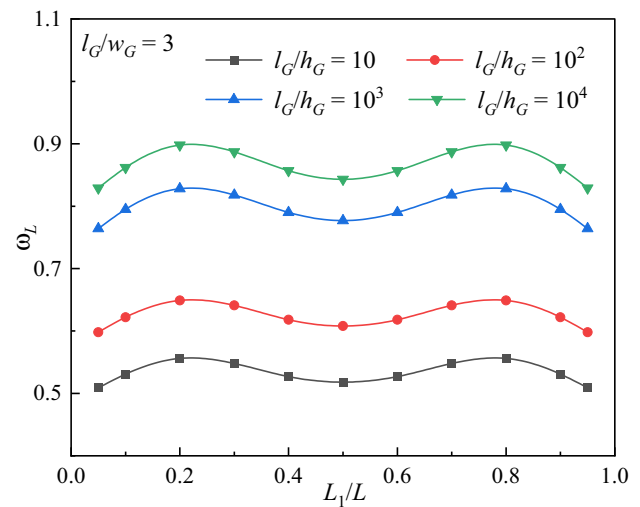

Fig. 6 Effects of the crack location and length-to-thickness ratio for the GPLs on the linear fundamental frequency of the edge-cracked C–C X-GRC piezoelectric beam

Table 7 Effect of applied actuator voltage on the linear fundamental frequencies of the edge-cracked FG-GRC piezoelectric beam under different boundary conditions

Boundary	V_0	U	FG-O	FG-X
C–C	−400	0.7430398	0.6466119	0.8178760
	0	0.7430394	0.6466114	0.8178755
	400	0.7430389	0.6466110	0.8178752
C–H	−400	0.5241995	0.4539933	0.5794602
	0	0.5241990	0.4539927	0.5794597
	400	0.5241984	0.4539921	0.5794592
H–H	−400	0.3307945	0.2843329	0.3659624
	0	0.3307938	0.2843320	0.3659618
	400	0.3307931	0.2843312	0.3659612

The direct iterative method [45] is used to analyze the mechanical–electrical vibration behaviors of the edge-cracked FG-GRC piezoelectric beam. Some steps are given as follows:

(1) Neglecting the nonlinear stiffness matrices $\mathbf{K}_{NL1}$ and $\mathbf{K}_{NL2}$ in Eq. (54), the linear eigenvalue and corresponding eigenvector are obtained.
(2) Scaled the obtained eigenvector to make that the largest transverse displacement equals to the given vibration amplitude.
(3) Updating the nonlinear stiffness matrices $\mathbf{K}_{NL1}$ and $\mathbf{K}_{NL2}$ by the scaled eigenvector in Eq. (54), the new eigenvalue and eigenvector are calculated by solving the updated eigensystem (54).

(4) Repeating the steps (2) and (3) until the relative error is less than 10^{-4} between the eigenvalues calculated by two successive iterations.

4 Results and discussion

In the following calculations, the FG-GRC beam is made of the epoxy and GPLs, and the piezoelectric layers are made by the polyvinylidene fluoride (PVDF). Table 1 gives the properties of the selected materials [38, 53]. Unless otherwise stated, the edge-cracked FG-GRC piezoelectric beam with $a/h = 0.3$ and $L_1/L = 0.5$ subjected to the applied actuator voltage $V_0 = 400$ V has the slender ratio $L/H = 10$. The thicknesses of the FG-GRC beam and the piezoelectric layer are, respectively, $h = 0.1$ m and $h_P = 0.01$ m. The length, width, and thickness of the GPLs are, respectively, $l_G = 2.5\ \mu m$, $w_G = 1.5\ \mu m$, and $h_G = 1.5$ nm, and the GPL weight fraction is $f_G = 0.5\%$.

4.1 Convergence and comparison

To check the convergence of the present analyses, Table 2 compares the linear fundamental frequency ω_L and nonlinear fundamental frequency ω_{NL} of the edge-cracked X-GRC piezoelectric beam with different boundary conditions and varying total number N of the GRC layers. Table 3 presents the effect of the polynomial terms n in Eqs. (46)–(52) on the linear fundamental frequency of the edge-cracked X-GRC piezoelectric beam. It is demonstrated that the linear and nonlinear fundamental frequencies increase firstly and tend to the constants as the increasing of the total number N and
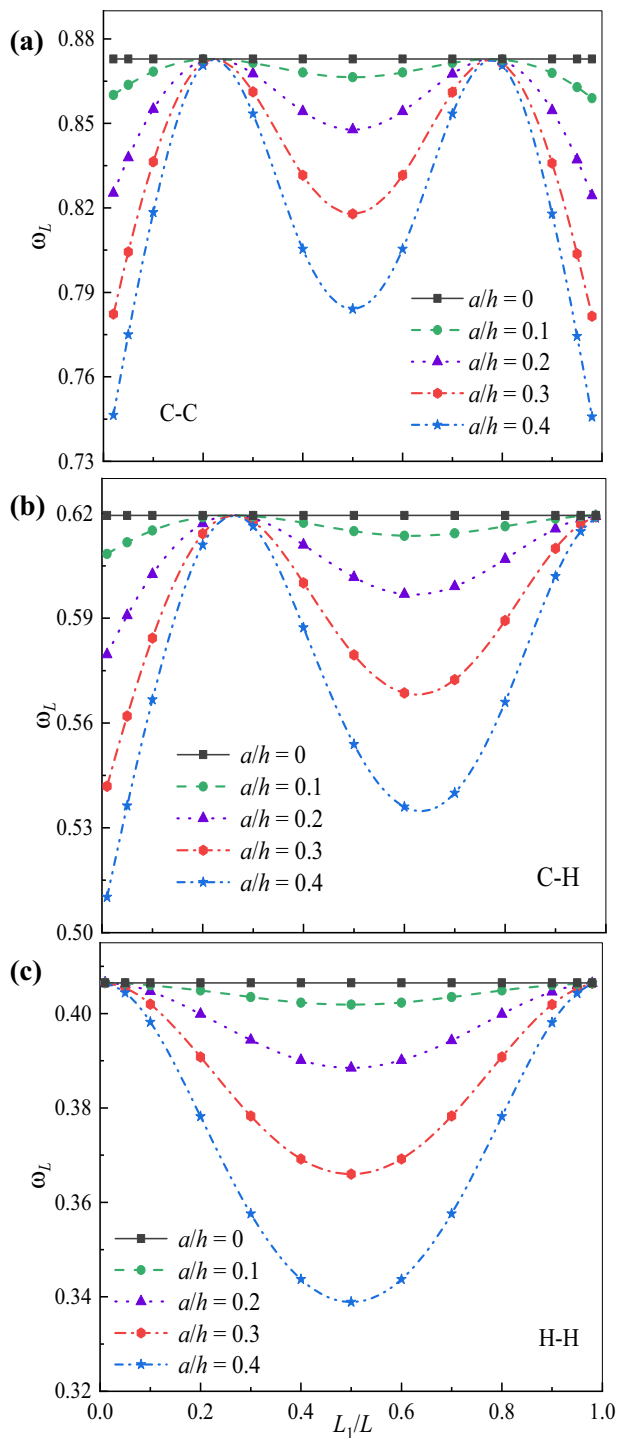
Fig. 7 Effects of the crack depth on the linear natural frequencies of the edge-cracked X-GRC piezoelectric beam under different boundary conditions, **a** C–C boundary, **b** C–H boundary, **c** H–H boundary
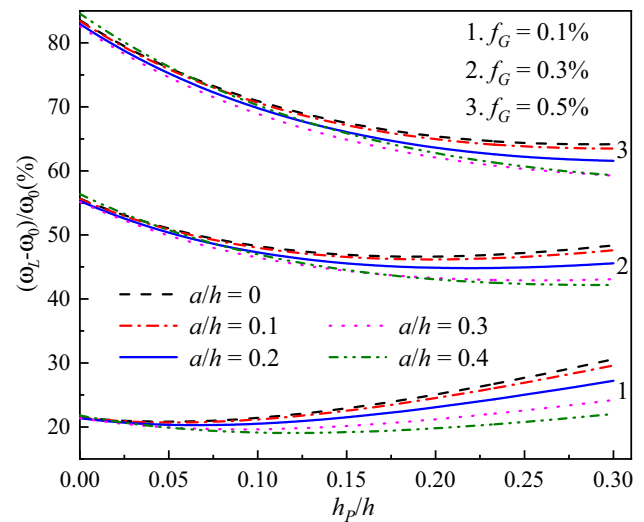

Fig. 8 Effects of the crack depth and thickness of piezoelectric layers on the linear frequency change ratio of the edge-cracked C–C X-GRC piezoelectric beam with different GPL weight fractions

In order to analyze the vibrations of the edge-cracked FG-GRC piezoelectric beam, some validations are presented in Tables 4, 5 and 6. Table 4 lists the dimensionless fundamental frequency ω_{NL} of the nonlinear vibrations for the GPL/epoxy composite beam with $f_G = 0.5\%$, $h = 0.1$ m, and $L/h = 20$. As a comparison, Feng et al.'s results [21] are also given in Table 4. Table 5 gives the linear fundamental frequency ratios of the edge-cracked FG-GRC beam with $f_G = 0.6\%$, $h = 0.12$ m, $L/h = 10$, and $a/h = 0.3$ under different crack locations which is reported by Song et al. [38]. Table 6 presents the frequency ratio of the nonlinear to linear vibrations ω_{NL}/ω_L for the carbon nanotube reinforced FG Euler piezoelectric beam with $V_{CN} = 17\%$, $L/H = 20$, $h = 80$ mm, $h_P/h = 1/8$, and $V_0 = 0$ under different CNT distribution patterns. Table 6 also gives Rafiee's results [52] as a comparison result. The difference between the present results and other results is acceptable. The present approach is feasibility to study the linear and nonlinear vibrations of the edge-cracked FG-GRC piezoelectric beam.

4.2 Linear vibration analyses

The linear vibration behaviors are analyzed for the edge-cracked FG-GRC piezoelectric beam. The influences of the GPL weight fractions, boundary conditions, GPL distribution patterns, applied actuator voltage, crack location, crack depth, and thickness of the piezoelectric layer on the linear vibration frequencies of the edge-cracked FG-GRC piezoelectric beam are presented in the diagrams and tabulations.

Figure 2 gives the effect of the thickness for the piezoelectric layer h_P with $h_P/h = 0$, 1/30, 1/20, and 1/10 on the first three mode shapes of the edge-cracked X-GRC piezoelectric

polynomial terms n. Considering the accuracy and efficiency of the calculations, the total number N of the GRC layers and number n of the polynomial terms are, respectively, taken as 10 and 5.

beam with the C–C boundary conditions. $h_P/h = 0$ implies that the edge-cracked X-GRC beam has no any piezoelectric layers. It is illustrated that all amplitudes of the first three mode shapes decrease with the increasing thickness of the piezoelectric layer. It is found that the piezoelectric layer can help us reduce the vibration of the edge-cracked X-GRC beam.

Figure 3 demonstrates the effects of the boundary conditions C–C, C–H, and H–H and GPL distribution patterns U, FG-O, and FG-X on the linear fundamental frequencies ω_L of the edge-cracked FG-GRC piezoelectric beam. It is predicted that the C–C edge-cracked FG-GRC piezoelectric beam has the largest linear fundamental frequency ω_L, and the linear fundamental frequency of the C–H edge-cracked FG-GRC piezoelectric beam is larger than that of the H–H edge-cracked FG-GRC piezoelectric beam. Based on different GPL distribution patterns, all GPL distribution patterns can obviously raise the natural frequency ω_L of the edge-cracked FG-GRC piezoelectric beam. Therefore, the FG-X pattern is the best one to improve the linear fundamental frequency ω_L of the edge-cracked FG-GRC piezoelectric beam, and the U and FG-O patterns take the second place. It is because more GPLs distribution into the upper and bottom layers can better enhance the stiffness of the edge-cracked epoxy piezoelectric beam.

Figure 4 shows the effect of the GPL distribution patterns on the linear fundamental frequency change ratio $(\omega_L - \omega_0)/\omega_0$ of the edge-cracked C–C FG-GRC piezoelectric beam with varying GPL weight fractions $f_G = 0.1\%$, 0.3%, and 0.5%, where ω_0 represents the linear fundamental frequency of the edge-cracked epoxy piezoelectric beam without any GPLs. The change ratio of the linear fundamental frequency significantly increases through increasing a little of the GPLs to the polymer matrix. For example, the linear fundamental frequency of the edge-cracked X-GRC piezoelectric beam increases to 15.7% through adding the very low GPL weight fraction $f_G = 0.1\%$ and further significantly increases as f_G increases. This clearly demonstrates that GPLs can effectively improve the stiffness of the epoxy piezoelectric beam.

Figure 5 gives the effects of the GPL weight fractions f_G on the change ratio $(\omega_L - \omega_0)/\omega_0$ of the linear fundamental frequency for the C–C X-GRC piezoelectric beam with different edge-crack depths. It is same with Fig. 4 that the change ratios of the fundamental frequency $(\omega_L - \omega_0)/\omega_0$ increase with the increase of the GPL weight fraction f_G. However, the frequency change ratio $(\omega_L - \omega_0)/\omega_0$ changes little with the varying crack depth. It is implied that the effect of the enhancement for the GPLs on the stiffness of the X-GRC piezoelectric beam is independent on the edge-crack depth.

Table 7 lists the linear fundamental frequency ω_L of the edge-cracked FG-GRC piezoelectric beam subjected to different applied actuator voltages V_0 and different boundary conditions. It is again proved that the FG-X distribution pattern is the best one for improving the vibration properties of the edge-cracked FG-GRC piezoelectric beam. It is observed that the frequency is almost unchanged with the increase of the applied actuator voltage V_0. It is noticed that the applied actuator voltage affects the vibration properties of the edge-cracked FG-GRC piezoelectric beam through the electric related loadings N_P and M_P, which are calculated by Eq. (25). The piezoelectric strain constant d_{31} in Eq. (25) is too small to give the notable electric related loadings.

Figure 6 presents the influences of the crack location L_1/L and length-to-thickness ratio l_G/h_G for the GPLs on the linear fundamental frequencies ω_L of the edge-cracked C–C X-GRC piezoelectric beam with $l_G/w_G = 3$. It is obviously found that the linear fundamental frequencies increase with the increasing length-to-thickness ratio l_G/h_G for the GPLs, which demonstrates that the GPLs with bigger surface area can lead to higher structural stiffness of the edge-cracked C–C X-GRC piezoelectric beam. However, the effect of the crack location on the linear fundamental frequency is independent of the varying length-to-thickness ratio l_G/h_G for the GPLs.

Figure 7 gives the effects of the crack depth on the linear natural frequencies ω_L of the edge-cracked X-GRC piezoelectric beams for different boundary conditions. It is shown that the deeper the crack is, the more sensitive the linear natural frequency ω_L is to the location of the crack for the edge-cracked X-GRC piezoelectric beams for different boundary conditions. Due to the symmetry of the C–C and H–H boundaries, the influences of the crack location on the linear natural frequency ω_L are symmetric with $X = 0.5$ for the edge-cracked X-GRC piezoelectric beams. For the H–H edge-cracked X-GRC piezoelectric beam, the crack located in the middle of the beam reduces the linear natural frequency. For the beam with the C–C boundaries, the edge-cracked X-GRC piezoelectric beam has the lowest linear natural frequency when the crack is near the clamped ends. Generally, the linear natural frequency decreases with the increasing depth of the crack. It is interesting that there are some positions in which the varying crack depth has no the effect on the linear natural frequency ω_L of the edge-cracked X-GRC piezoelectric beam with the C–C and C–H boundaries.

Figure 8 depicts the influences of the crack depth and thickness of the piezoelectric layers on the change ratios of the linear natural frequency $(\omega_L - \omega_{01})/\omega_{01}$ of the edge-cracked C–C X-GRC piezoelectric beams with different GPL weight fractions, where ω_{01} is the linear fundamental frequency of the edge-cracked pure epoxy beam without the piezoelectric layers. The deeper the crack is, the lower the change ratio of the linear frequency $(\omega_L - \omega_{01})/\omega_{01}$ is. The linear frequency change ratio $(\omega_L - \omega_{01})/\omega_{01}$ decreases firstly and then increases with the increasing thickness of piezoelectric layer for the lower GPL weight fractions $f_G = 0.1\%$ and $f_G = 0.3\%$. It is shown that

Table 8 Effect of applied actuator voltage on the nonlinear fundamental frequency ratios of the edge-cracked FG-GRC piezoelectric beam

Boundary	V_0 (V)	U	FG-O	FG-X
C–C	−400	1.1062117	1.1389347	1.0884601
	0	1.1062119	1.1389349	1.0884602
	400	1.1062121	1.1389350	1.0884598
C–H	−400	1.2482830	1.3214721	1.2069442
	0	1.2482834	1.3214729	1.2069445
	400	1.2482839	1.3214738	1.2069448
H–H	−400	1.4326186	1.5567592	1.3644425
	0	1.4326205	1.5567616	1.3644435
	400	1.4326218	1.5567644	1.3644446

Fig. 10 Effect of the GPL weight fraction on the nonlinear fundamental frequency ratio for the edge-cracked C–C X-GRC piezoelectric beam
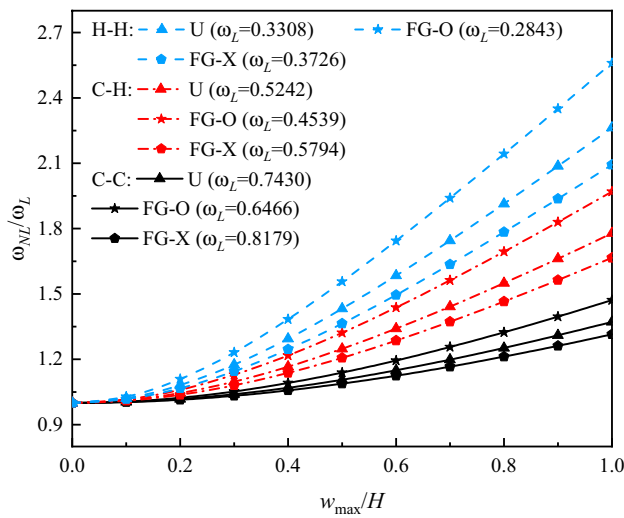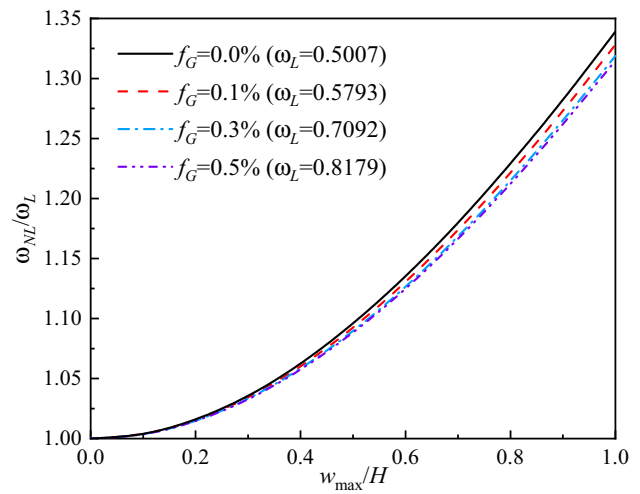

Fig. 9 Effects of the GPL distributions and boundary conditions on the nonlinear fundamental frequency ratios of the edge-cracked FG-GRC piezoelectric beam
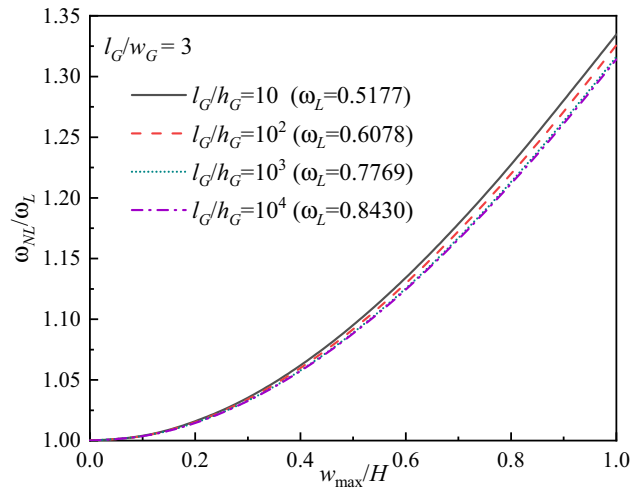

Fig. 11 Effect of the length-to-thickness ratio for GPLs on nonlinear fundamental frequency ratio of the edge-cracked C–C X-GRC piezoelectric beam

there is different trend to the edge-cracked X-GRC piezoelectric beam with the GPL weight fraction $f_G = 0.5\%$, in which the linear frequency change ratio $(\omega_L - \omega_{01})/\omega_{01}$ decreases with the increasing thickness of piezoelectric layer. When the thickness ratio h_P/h increases and is bigger than 0.4, the linear frequency change ratio $(\omega_L - \omega_{01})/\omega_{01}$ raises with the growing thickness ratio h_P/h.

4.3 Nonlinear vibration analyses

The nonlinear vibration behaviors are discussed for the edge-cracked FG-GRC piezoelectric beam. Different distribution patterns, weight fractions and geometry characteristic of the GPLs, thickness of the piezoelectric layers, applied actuator voltage, as well as the crack depth are considered.

Table 8 gives the influences of the applied actuator voltage on the nonlinear frequency ratios ω_{NL}/ω_L of the edge-cracked

FG-GRC piezoelectric beam. For a given boundary, the FG-X and FG-O distributions, respectively, have the lowest and highest nonlinear frequency ratios ω_{NL}/ω_L. For a given GPL pattern, the edge-cracked FG-GRC piezoelectric beams under the C–C and H–H boundaries, respectively, have the smallest and largest nonlinear vibration frequency ratios. Besides, similar with observed in Table 7 for the linear vibration of the edge-cracked FG-GRC piezoelectric beam, the nonlinear vibration frequency ω_{NL} is insensitive to the varying applied actuator voltage.

Figure 9 indicates the nonlinear frequency ratio ω_{NL}/ω_L of the edge-cracked FG-GRC piezoelectric beam with varying boundary conditions C–C, C–H, and H–H under different GPL distribution patterns U, FG-O and FG-X. For
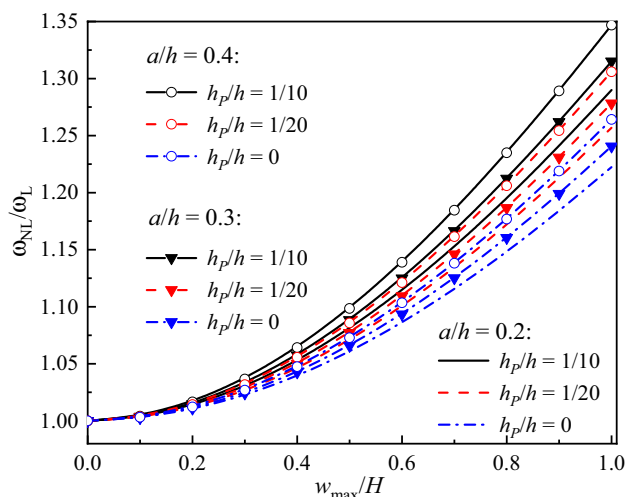
Fig. 12 Effect of the crack depth on the nonlinear frequency ratio for the edge-cracked C–C X-GRC piezoelectric beam of varying thickness

the hard-spring characteristic of the system, the nonlinear vibration frequency ratio ω_{NL}/ω_L increases with the increasing nonlinear vibration amplitude. The weaker the boundary condition is, the clearer the hard-spring characteristic is.

Figures 10 and 11, respectively, demonstrate the effects of the GPL weight fractions f_G and length-to-thickness ratios l_G/h_G of the GPLs on the nonlinear frequency ratios ω_{NL}/ω_L of the edge-cracked C–C X-GRC piezoelectric beam. The nonlinear frequency ratio is also plotted for the pure epoxy beam with the piezoelectric layers and the GPL weight fraction $f_G = 0$, as shown in Fig. 10. We see that the nonlinear frequency ratios ω_{NL}/ω_L increase with the increase of the vibration amplitude for all cases. In addition, the nonlinear frequency ratios ω_{NL}/ω_L decrease with the raises of the GPL weight fraction f_G and GPL length-to-thickness ratio l_G/h_G.

Figure 12 denotes the effects of the crack depth sizes $a/h = 0.2$, 0.3, and 0.4 on the nonlinear frequency ratios ω_{NL}/ω_L of the edge-cracked C–C X-GRC piezoelectric beams with varying thickness sizes $h_P/h = 0$, 1/20, and 1/10. For the given crack depth, the increasing thickness of the piezoelectric layers leads to enhance the nonlinear frequency ratio ω_{NL}/ω_L of the edge-cracked C–C X-GRC piezoelectric beam. For the certain thickness of the piezoelectric layers, the deeper the crack is, the larger the nonlinear frequency ratios ω_{NL}/ω_L are for the edge-cracked C–C X-GRC piezoelectric beam.

5 Conclusions

The mechanical–electrical vibrations of the edge-cracked FG-GRC beam covered by the piezoelectric layers have been investigated based on Timoshenko beam theory

and Ritz method. A rotational massless spring model is obtained to simulate the open edge crack. The effects of the boundary condition, distribution patterns and weight fractions of the GPLs, depth and location of the crack, thickness of the piezoelectric actuator, and applied actuator voltage on the linear and nonlinear vibrations of the edge-cracked FG-GRC piezoelectric beam are numerically investigated. The obtained results are given as follows:

(1) The stiffness of the edge-cracked epoxy piezoelectric beam can be significantly improved by using a little amount of the GPLs, especially the big surface area of the GPLs. The effect of the GPLs on the stiffness of the edge-cracked FG-GRC piezoelectric beam is independent on the edge-crack depth.

(2) For the symmetric boundaries, the influence of the crack location on the linear natural frequency of the edge-cracked FG-GRC piezoelectric beam is symmetric. For the clamped boundaries, there are some positions in which the varying crack depth has no the effect on the linear natural frequency of the edge-cracked FG-GRC piezoelectric beam.

(3) There exists a critical thickness of the piezoelectric layer. Below the critical thickness, the natural frequencies of the edge-cracked X-GRC piezoelectric beam decrease with the increase of the thickness for the piezoelectric layer. However, upon critical thickness, the natural frequency of the edge-cracked X-GRC piezoelectric beam increases with the increase of the thickness for the piezoelectric layer.

Appendix A

The trail functions in Eqs. (48)–(52) are expressed in the following forms:

$$U_a(X) = \sum_{j=1}^{n} A_j H_{1j}, \quad W_a(X) = \sum_{j=1}^{n} B_j H_{1j},$$

$$U_b(X) = \sum_{j=1}^{n} \tilde{A}_j H_{2j}, \quad W_b(X) = \sum_{j=1}^{n} \tilde{B}_j H_{2j},$$

$$U_2(X) = \sum_{j=1}^{n} \tilde{A}_j H_{3j}, \quad W_2(X) = \sum_{j=1}^{n} \tilde{B}_j H_{3j}, \tag{55}$$

$$\psi_a(X) = \sum_{j=1}^{n} C_j H_{4j}, \quad \psi_b(X) = \sum_{j=1}^{n} \tilde{C}_j H_{5j}, \text{ and}$$

$$\psi_c(X) = \sum_{j=1}^{n} \tilde{A}_j H_{6j}, \quad \psi_2(X) = \sum_{j=1}^{n} \tilde{C}_j H_{7j}.$$

Appendix B

The elements of symmetric linear stiffness matrix $\mathbf{K_L}$ in Eq. (54) are

$$\mathbf{K}_{\mathbf{L}(j,m)} = \int_0^{X_0} \left(a_{11} \frac{\partial H_{1j}}{\partial X} \frac{\partial H_{1m}}{\partial X} \right) dX, \ \mathbf{K}_{\mathbf{L}(j,n+m)} = \int_0^{X_0} \left(a_{11} \frac{\partial H_{1j}}{\partial X} \frac{\partial H_{2m}}{\partial X} + b_{11} \frac{\partial H_{1j}}{\partial X} \frac{\partial H_{6m}}{\partial X} \right) dX,$$

$$\mathbf{K}_{\mathbf{L}(j,2n+m)} = \mathbf{K}_{\mathbf{L}(j,3n+m)} = 0, \ \mathbf{K}_{\mathbf{L}(j,4n+m)} = \int_0^{X_0} \left(b_{11} \frac{\partial H_{1j}}{\partial X} \frac{\partial H_{4m}}{\partial X} \right) dX,$$

$$\mathbf{K}_{\mathbf{L}(j,5n+m)} = \int_0^{X_0} \left(b_{11} \frac{\partial H_{1j}}{\partial X} \frac{\partial H_{5m}}{\partial X} \right) dX,$$

$$\mathbf{K}_{\mathbf{L}(n+j,n+m)} = \int_0^{X_0} \left[a_{11} \frac{\partial H_{2j}}{\partial X} \frac{\partial H_{2m}}{\partial X} + b_{11} \left(\frac{\partial H_{2j}}{\partial X} \frac{\partial H_{6m}}{\partial X} + \frac{\partial H_{2m}}{\partial X} \frac{\partial H_{6j}}{\partial X} \right) + d_{11} \frac{\partial H_{6j}}{\partial X} \frac{\partial H_{6m}}{\partial X} \right.$$

$$\left. + a_{55} \eta^2 H_{6j} H_{6m} \right] dX + \int_{X_0}^1 \left(a_{11} \frac{\partial H_{3j}}{\partial X} \frac{\partial H_{3m}}{\partial X} \right) dX + K_T^* \left(H_{6j} H_{6m} \right)_{X=X_0},$$

$$\mathbf{K}_{\mathbf{L}(n+j,2n+m)} = \int_0^{X_0} \left(a_{55} \eta H_{6j} \frac{\partial H_{1m}}{\partial X} \right) dX, \ \mathbf{K}_{\mathbf{L}(n+j,3n+m)} = \int_0^{X_0} \left(a_{55} \eta H_{6j} \frac{\partial H_{2m}}{\partial X} \right) dX,$$

$$\mathbf{K}_{\mathbf{L}(n+j,4n+m)} = \int_0^{X_0} \left(b_{11} \frac{\partial H_{2j}}{\partial X} \frac{\partial H_{4m}}{\partial X} + d_{11} \frac{\partial H_{6j}}{\partial X} \frac{\partial H_{4m}}{\partial X} + a_{55} \eta^2 H_{6j} H_{4m} \right) dX + K_T^* \left(H_{6j} H_{4m} \right)_{X=X_0},$$

$$\mathbf{K}_{\mathbf{L}(n+j,5n+m)} = \int_0^{X_0} \left(b_{11} \frac{\partial H_{2j}}{\partial X} \frac{\partial H_{5m}}{\partial X} + d_{11} \frac{\partial H_{6j}}{\partial X} \frac{\partial H_{5m}}{\partial X} + a_{55} \eta^2 H_{6j} H_{5m} \right) dX$$

$$+ \int_{X_0}^1 \left(b_{11} \frac{\partial H_{3j}}{\partial X} \frac{\partial H_{7m}}{\partial X} \right) dX + K_T^* \left(H_{6j} H_{5m} - H_{6j} H_{7m} \right)_{X=X_0},$$

$$\mathbf{K}_{\mathbf{L}(2n+j,2n+m)} = \int_0^{X_0} \left(a_{55} \frac{\partial H_{1j}}{\partial X} \frac{\partial H_{1m}}{\partial X} - \frac{1}{2} \tilde{N}^P \frac{\partial H_{1j}}{\partial X} \frac{\partial H_{1m}}{\partial X} \right) dX, \tag{56}$$

$$\mathbf{K}_{\mathbf{L}(2n+j,3n+m)} = \int_0^{X_0} \left(a_{55} \frac{\partial H_{1j}}{\partial X} \frac{\partial H_{2m}}{\partial X} - \frac{1}{2} \tilde{N}^P \frac{\partial H_{1j}}{\partial X} \frac{\partial H_{2m}}{\partial X} \right) dX,$$

$$\mathbf{K}_{\mathbf{L}(2n+j,4n+m)} = \int_0^{X_0} \left(a_{55} \eta \frac{\partial H_{1j}}{\partial X} H_{4m} \right) dX, \ \mathbf{K}_{\mathbf{L}(2n+j,5n+m)} = \int_0^{X_0} \left(a_{55} \eta \frac{\partial H_{1j}}{\partial X} H_{5m} \right) dX,$$

$$\mathbf{K}_{\mathbf{L}(3n+j,3n+m)} = \int_0^{X_0} \left(a_{55} \frac{\partial H_{2j}}{\partial X} \frac{\partial H_{2m}}{\partial X} - \frac{1}{2} \tilde{N}^P \frac{\partial H_{2j}}{\partial X} \frac{\partial H_{2m}}{\partial X} \right) dX$$

$$+ \int_{X_0}^1 \left(a_{55} \frac{\partial H_{3j}}{\partial X} \frac{\partial H_{3m}}{\partial X} - \frac{1}{2} \tilde{N}^P \frac{\partial H_{3j}}{\partial X} \frac{\partial H_{3m}}{\partial X} \right) dX,$$

$$\mathbf{K}_{\mathbf{L}(3n+j,4n+m)} = \int_0^{X_0} \left(a_{55} \frac{\partial H_{2j}}{\partial X} H_{4m} \right) dX,$$

$$\mathbf{K}_{\mathbf{L}(3n+j,5n+m)} = \int_0^{X_0} \left(a_{55} \frac{\partial H_{2j}}{\partial X} H_{5m} + a_{55} \frac{\partial H_{3j}}{\partial X} H_{7m} \right) dX,$$

$$\mathbf{K}_{\mathbf{L}(4n+j,4n+m)} = \int_0^{X_0} \left(d_{11} \frac{\partial H_{4j}}{\partial X} \frac{\partial H_{4m}}{\partial X} + a_{55} \eta^2 H_{4j} H_{4m} \right) dX + K_T^* \left(H_{4j} H_{4m} \right)_{X=X_0},$$

$$\mathbf{K}_{\mathbf{L}(4n+j,5n+m)} = \int_0^{X_0} \left(d_{11} \frac{\partial H_{4j}}{\partial X} \frac{\partial H_{5m}}{\partial X} + a_{55} \eta^2 H_{4j} H_{5m} \right) dX + K_T^* \left(H_{4j} H_{5m} - H_{4j} H_{7m} \right)_{X=X_0}, \text{ and}$$

$$\mathbf{K}_{\mathbf{L}(5n+j,5n+m)} = \int_0^{X_0} \left(d_{11} \frac{\partial H_{5j}}{\partial X} \frac{\partial H_{5m}}{\partial X} + a_{55} \eta^2 H_{5j} H_{5m} \right) dX + \int_{X_0}^1 \left(d_{11} \frac{\partial H_{7j}}{\partial X} \frac{\partial H_{7m}}{\partial X} + a_{55} \eta^2 H_{7j} H_{7m} \right) dX$$

$$+ K_T^* \left(H_{7j} H_{7m} + H_{5j} H_{5m} - H_{5j} H_{7m} - H_{7j} H_{5m} \right)_{X=X_0}.$$

The elements of the symmetric mass matrix $\mathbf{M}$ in Eq. (54) are

$$\mathbf{M}_{(j,m)} = \int_0^{X_0} \tilde{I}_1 H_{1j} H_{1m} dX, \ \mathbf{M}_{(j,n+m)} = \int_0^{X_0} \left(\tilde{I}_1 H_{1j} H_{2m} + \tilde{I}_2 H_{1j} H_{6m} \right) dX,$$

$$\mathbf{M}_{(j,2n+m)} = \mathbf{M}_{(j,3n+m)} = 0, \ \mathbf{M}_{(j,4n+m)} = \int_0^{X_0} \tilde{I}_2 H_{1j} H_{4m} dX, \ \mathbf{M}_{(j,5n+m)} = \int_0^{X_0} \tilde{I}_2 H_{1j} H_{5m} dX,$$

$$\mathbf{M}_{(n+j,n+m)} = \int_0^{X_0} \left(\tilde{I}_1 H_{2j} H_{2m} + \tilde{I}_2 H_{2j} H_{6m} + \tilde{I}_2 H_{2m} H_{6j} + \tilde{I}_3 H_{6j} H_{6m} \right) dX + \int_{X_0}^1 \tilde{I}_1 H_{3j} H_{3m} dX,$$

$$\mathbf{M}_{(n+j,2n+m)} = \mathbf{M}_{(n+j,3n+m)} = 0, \ \mathbf{M}_{(n+j,4n+m)} = \int_0^{X_0} \left(\tilde{I}_2 H_{2j} H_{4m} + \tilde{I}_3 H_{6j} H_{4m} \right) dX,$$

$$\mathbf{M}_{(n+j,5n+m)} = \int_0^{X_0} \left(\tilde{I}_2 H_{2j} H_{5m} + \tilde{I}_3 H_{6j} H_{5m} \right) dX + \int_{X_0}^1 \tilde{I}_2 H_{3j} H_{7m} dX, \tag{57}$$

$$\mathbf{M}_{(2n+j,2n+m)} = \int_0^{X_0} \tilde{I}_1 H_{1j} H_{1m} dX, \ \mathbf{M}_{(2n+j,3n+m)} = \int_0^{X_0} \tilde{I}_1 H_{1j} H_{2m} dX,$$

$$\mathbf{M}_{(2n+j,4n+m)} = \mathbf{M}_{(2n+j,5n+m)} = 0, \ \mathbf{M}_{(3n+j,3n+m)} = \int_0^{X_0} \tilde{I}_1 H_{2j} H_{2m} dX + \int_{X_0}^1 \tilde{I}_1 H_{3j} H_{3m} dX,$$

$$\mathbf{M}_{(3n+j,4n+m)} = \mathbf{M}_{(3n+j,5n+m)} = 0, \ \mathbf{M}_{(4n+j,4n+m)} = \int_0^{X_0} \tilde{I}_3 H_{4j} H_{4m} dX, \text{ and}$$

$$\mathbf{M}_{(4n+j,5n+m)} = \int_0^{X_0} \tilde{I}_3 H_{4j} H_{5m} dX, \ \mathbf{M}_{(5n+j,5n+m)} = \int_0^{X_0} \tilde{I}_3 H_{5j} H_{5m} dX + \int_{X_0}^1 \tilde{I}_3 H_{7j} H_{7m} dX.$$

The elements of the nonlinear stiffness matrices matrix $\mathbf{K}_{\mathbf{NL}1}$ and $\mathbf{K}_{\mathbf{NL}2}$ in Eq. (54) are given as

$$\mathbf{K}_{\mathbf{NL}1(j,m)} = \mathbf{K}_{\mathbf{NL}1(j,n+m)} = 0, \ \mathbf{K}_{\mathbf{NL}1(j,2n+m)} = \int_0^{X_0} \left(\frac{a_{11}}{\eta} \frac{\partial W_1}{\partial X} \frac{\partial H_{1j}}{\partial X} \frac{\partial H_{1m}}{\partial X} \right) dX,$$

$$\mathbf{K}_{\mathbf{NL}1(j,3n+m)} = \int_0^{X_0} \left(\frac{a_{11}}{\eta} \frac{\partial W_1}{\partial X} \frac{\partial H_{1j}}{\partial X} \frac{\partial H_{2m}}{\partial X} \right) dX, \ \mathbf{K}_{\mathbf{NL}1(j,4n+m)} = \mathbf{K}_{\mathbf{NL}1(j,5n+m)} = \mathbf{K}_{\mathbf{NL}1(n+j,n+m)} = 0,$$

$$\mathbf{K}_{\mathbf{NL}1(n+j,2n+m)} = \int_0^{X_0} \left(\frac{a_{11}}{\eta} \frac{\partial W_1}{\partial X} \frac{\partial H_{2j}}{\partial X} \frac{\partial H_{1m}}{\partial X} + \frac{b_{11}}{\eta} \frac{\partial W_1}{\partial X} \frac{\partial H_{6j}}{\partial X} \frac{\partial H_{1m}}{\partial X} \right) dX,$$

$$\mathbf{K}_{\mathbf{NL}1(n+j,3n+m)} = \int_0^{X_0} \left(\frac{a_{11}}{\eta} \frac{\partial W_1}{\partial X} \frac{\partial H_{2j}}{\partial X} \frac{\partial H_{2m}}{\partial X} + \frac{b_{11}}{\eta} \frac{\partial W_1}{\partial X} \frac{\partial H_{6j}}{\partial X} \frac{\partial H_{2m}}{\partial X} \right) dX$$

$$+ \int_{X_0}^1 \left(\frac{a_{11}}{\eta} \frac{\partial W_2}{\partial X} \frac{\partial H_{3j}}{\partial X} \frac{\partial H_{3m}}{\partial X} \right) dX,$$

$$\mathbf{K}_{\mathbf{NL}1(n+j,4n+m)} = \mathbf{K}_{\mathbf{NL}1(n+j,5n+m)} = 0, \ \mathbf{K}_{\mathbf{NL}1(2n+j,2n+m)} = \int_0^{X_0} \frac{a_{11}}{\eta} \left(\frac{\partial U_1}{\partial X} + \frac{\partial \psi_1}{\partial X} \right) \frac{\partial H_{1j}}{\partial X} \frac{\partial H_{1m}}{\partial X} dX,$$

$$\mathbf{K}_{\mathbf{NL}1(2n+j,3n+m)} = \int_0^{X_0} \frac{a_{11}}{\eta} \left(\frac{\partial U_1}{\partial X} + \frac{\partial \psi_1}{\partial X} \right) \frac{\partial H_{1j}}{\partial X} \frac{\partial H_{2m}}{\partial X} dX,$$

$$\mathbf{K}_{\mathbf{NL}1(2n+j,4n+m)} = \int_0^{X_0} \left(\frac{b_{11}}{\eta} \frac{\partial W_1}{\partial X} \frac{\partial H_{1j}}{\partial X} \frac{\partial H_{4m}}{\partial X} \right) dX,$$

$$\mathbf{K}_{\mathbf{NL}1(2n+j,5n+m)} = \int_0^{X_0} \left(\frac{b_{11}}{\eta} \frac{\partial W_1}{\partial X} \frac{\partial H_{1j}}{\partial X} \frac{\partial H_{5m}}{\partial X} \right) dX, \ \mathbf{K}_{\mathbf{NL}1(3n+j,3n+m)} = 0, \tag{58}$$

$$\mathbf{K}_{\mathbf{NL}1(3n+j,4n+m)} = \int_0^{X_0} \left(\frac{b_{11}}{\eta} \frac{\partial W_1}{\partial X} \frac{\partial H_{2j}}{\partial X} \frac{\partial H_{4m}}{\partial X} \right) dX,$$

$$\mathbf{K}_{\mathbf{NL}1(3n+j,5n+m)} = \int_0^{X_0} \left(\frac{b_{11}}{\eta} \frac{\partial W_1}{\partial X} \frac{\partial H_{2j}}{\partial X} \frac{\partial H_{5m}}{\partial X} \right) dX + \int_{X_0}^1 \left(\frac{b_{11}}{\eta} \frac{\partial W_2}{\partial X} \frac{\partial H_{3j}}{\partial X} \frac{\partial H_{7m}}{\partial X} \right) dX,$$

$$\mathbf{K}_{\mathbf{NL}1(4n+j,4n+m)} = \mathbf{K}_{\mathbf{NL}1(4n+j,5n+m)} = \mathbf{K}_{\mathbf{NL}1(5n+j,5n+m)} = 0,$$

$$\mathbf{K}_{\mathbf{NL}2(j,m)} = \mathbf{K}_{\mathbf{NL}2(j,n+m)} = \mathbf{K}_{\mathbf{NL}2(j,2n+m)} = \mathbf{K}_{\mathbf{NL}2(j,3n+m)} = \mathbf{K}_{\mathbf{NL}2(j,4n+m)} = \mathbf{K}_{\mathbf{NL}2(j,5n+m)} = 0,$$

$$\mathbf{K}_{\mathbf{NL}2(n+j,m)} = \mathbf{K}_{\mathbf{NL}2(n+j,n+m)} = \mathbf{K}_{\mathbf{NL}2(n+j,2n+m)} = \mathbf{K}_{\mathbf{NL}2(n+j,3n+m)} = 0,$$

$$\mathbf{K}_{\mathbf{NL}2(n+j,4n+m)} = \mathbf{K}_{\mathbf{NL}2(n+j,5n+m)} = 0,$$

$$\mathbf{K}_{\mathbf{NL}2(2n+j,2n+m)} = \frac{3a_{11}}{2\eta^2} \int_0^{X_0} \left(\frac{\partial W_1}{\partial X} \right)^2 \frac{\partial H_{1j}}{\partial X} \frac{\partial H_{1m}}{\partial X} dX,$$

$$\mathbf{K}_{\mathbf{NL}2(2n+j,3n+m)} = \frac{3a_{11}}{2\eta^2} \int_0^{X_0} \left(\frac{\partial W_1}{\partial X} \right)^2 \frac{\partial H_{1j}}{\partial X} \frac{\partial H_{2m}}{\partial X} dX,$$

$$\mathbf{K}_{\mathbf{NL}2(2n+j,4n+m)} = \mathbf{K}_{\mathbf{NL}2(2n+j,5n+m)} = 0,$$

$$\mathbf{K}_{\mathbf{NL}2(3n+j,3n+m)} = \frac{3a_{11}}{2\eta^2} \int_0^{X_0} \left(\frac{\partial W_1}{\partial X} \right)^2 \frac{\partial H_{2j}}{\partial X} \frac{\partial H_{2m}}{\partial X} dX + \frac{3a_{11}}{2\eta^2} \int_{X_0}^1 \left(\frac{\partial W_2}{\partial X} \right)^2 \frac{\partial H_{3j}}{\partial X} \frac{\partial H_{3m}}{\partial X} dX, \text{ and}$$

$$\mathbf{K}_{\mathbf{NL}2(3n+j,4n+m)} = \mathbf{K}_{\mathbf{NL}2(3n+j,5n+m)} = \mathbf{K}_{\mathbf{NL}2(4n+j,4n+m)} = \mathbf{K}_{\mathbf{NL}2(4n+j,5n+m)} = \mathbf{K}_{\mathbf{NL}2(5n+j,5n+m)} = 0.$$

where $j, m = 1, 2, \ldots, n$.

Declarations

Conflict of interest The authors declare that there is no conflict of interests regarding the publication of this paper.

References

1. Novoselov KS, Geim AK, Morozov SV, Jiang D, Zhang Y, Dubonos SV, Grigorieva IV, Firsov AA (2004) Electric field effect in atomically thin carbon films. Science 306:666–669

2. Zaman I, Phan TT, Kuan HC, Meng Q, La LTB, Luong L, Youssf O, Ma J (2011) Epoxy/graphene platelets nanocomposites with two levels of interface strength. Polymer 52:1603–1611

3. Chen JH, Jang C, Xiao S, Ishigami M, Fuhrer MS (2008) Intrinsic and extrinsic performance limits of graphene devices on SiO_2. Nat Nanotechnol 3:206–209

4. Nieto A, Bisht A, Lahiri D, Zhang C, Agarwal A (2017) Graphene reinforced metal and ceramic matrix composites: a review. Int Mater Rev 62:241–302

5. Zhao S, Zhao Z, Yang Z, Ke L, Kitipornchai S, Yang J (2020) Functionally graded graphene reinforced composite structures: a review. Eng Struct 210:110339

6. Rafiee MA, Rafiee J, Wang Z, Song H, Yu ZZ, Koratkar N (2009) Enhanced mechanical properties of nanocomposites at low graphene content. ACS Nano 3:3884–3890

7. Guo XY, Jiang P, Zhang W, Yang J, Kitipornchai S, Sun L (2018) Nonlinear dynamic analysis of composite piezoelectric plates with graphene skin. Compos Struct 206:839–852

8. Guo LJ, Mao JJ, Zhang W (2021) Buckling analyses of edge-cracked functionally graded graphene reinforced composite piezoelectric beam. J Phys Conf Ser 1906:012042

9. Suresh S, Mortensen A (1998) Fundamentals of functionally graded materials. IOM Communications Ltd, London

10. Ke LL, Wang YS (2006) Two-dimensional contact mechanics of functionally graded materials with arbitrary spatial variations of material properties. Int J Solids Struct 43:5779–5798

11. Hao YX, Chen LH, Zhang W, Lei JG (2008) Nonlinear oscillations, bifurcations and chaos of functionally graded materials plate. J Sound Vib 312:862–892

12. Vel SS, Batra RC (2004) Three-dimensional exact solution for the vibration of functionally graded rectangular plates. J Sound Vib 272:703–730

13. Efraim E, Eisenberger M (2007) Exact vibration analysis of variable thickness thick annular isotropic and FGM plates. J Sound Vib 299:720–738

14. Zhang W, Yang J, Hao YX (2010) Chaotic vibrations of an orthotropic FGM rectangular plate based on third-order shear deformation theory. Nonlinear Dyn 59:619–660

15. Mao JJ, Ke LL, Wang YS, Liu J (2016) Frictionally excited thermoelastic instability of functionally graded materials sliding out-of-plane with contact resistance. J Appl Mech Trans ASME 83:021010

16. Cao DX, Gao YH, Yao MH, Zhang W (2018) Free vibration of axially functionally graded beams using the asymptotic development method. Eng Struct 173:442–448

17. Abo-Bakr RM, Eltaher MA, Atti MA (2020) Pull-in and free-standing instability of actuated functionally graded nanobeams including surface and stiffening effects. Eng Comput. https://doi.org/10.1007/s00366-020-01146-0

18. Esen I, Abdelrhmaan AA, Eltaher MA (2021) Free vibration and buckling stability of FG nanobeams exposed to magnetic and thermal fields. Eng Comput. https://doi.org/10.1007/s00366-021-01389-5

19. Hamed MA, Abo-Bakr RM, Mohamed SA, Eltaher MA (2020) Influence of axial load function and optimization on static stability of sandwich functionally graded beams with porous core. Eng Comput 36:1929–1946

20. Daikh AA, Houari MSA, Belarbi MO, Chakraverty S, Eltaher MA (2021) Analysis of axially temperature-dependent functionally graded carbon nanotube reinforced composite plates. Eng Comput. https://doi.org/10.1007/s00366-021-01413-8

21. Feng C, Kitipornchai S, Yang J (2017) Nonlinear free vibration of functionally graded polymer composite beams reinforced with graphene nanoplatelets (GPLs). Eng Struct 140:110–119

22. Song MT, Kitipornchai S, Yang J (2017) Free and forced vibrations of functionally graded polymer composite plates reinforced with graphene nanoplatelets. Compos Struct 159:579–588

23. Shen HS, Xiang Y, Fan Y (2019) Nonlinear vibration of thermally postbuckled FG-GRC laminated beams resting on elastic foundations. Int J Struct Stab Dyn. https://doi.org/10.1142/S0219455419500512

24. Shen HS, Xian Y, Fan Y, Hui D (2018) Nonlinear vibration of functionally graded graphene-reinforced composite laminated cylindrical panels resting on elastic foundations in thermal environments. Compos Part B Eng 136:177–186

25. Mao JJ, Zhang W (2019) Buckling and post-buckling analyses of functionally graded graphene reinforced piezoelectric plate subjected to electric potential and axial forces. Compos Struct 216:392–405

26. Mao JJ, Zhang W (2018) Linear and nonlinear free and forced vibrations of graphene reinforced piezoelectric composite plate under external voltage excitation. Compos Struct 203:551–565

27. Wang YW, Xie K, Fu T, Zhang W (2021) A third order shear deformable model and its applications for nonlinear dynamic response of graphene oxides reinforced curved beams resting on visco-elastic foundation and subjected to moving loads. Eng Comput. https://doi.org/10.1007/s00366-020-01238-x

28. Wang AW, Chen HY, Hao YX, Zhang W (2018) Vibration and bending behavior of functionally graded nanocomposite doubly-curved shallow shells reinforced by graphene nanoplatelets. Results Phys 9:550–559

29. Mohamed N, Mohamed SA, Eltaher MA (2021) Buckling and post-buckling behaviors of higher order carbon nanotubes using energy-equivalent model. Eng Comput 37:2823–2836

30. Esen I, Abdelrahman AA, Eltaher MA (2020) Dynamics analysis of Timoshenko perforated microbeams under moving loads. Eng Comput. https://doi.org/10.1007/s00366-020-01212-7

31. Mao JJ, Lu HM, Zhang W, Lai SK (2020) Vibrations of graphene nanoplatelet reinforced functionally gradient piezoelectric composite microplate based on nonlocal theory. Compos Struct 236:111813

32. Yang XD, Wang SW, Zhang W, Yang TZ, Lim CW (2018) Model formulation and modal analysis of a rotating elastic uniform Timoshenko beam with setting angle. Eur J Mech A Solids 72:209–222

33. Wu HL, Yang J, Kitipornchai S (2016) Nonlinear vibration of functionally graded carbon nanotube-reinforced composite beams with geometric imperfections. Compos Part B Eng 90:86–96

34. Rafiee M, He XQ, Liew KM (2014) Non-linear dynamic stability of piezoelectric functionally graded carbon nanotube-reinforced composite plates with initial geometric imperfection. Int J Nonlinear Mech 59:37–51

35. Dimarogonas AD (1996) Vibration of cracked structures: a state of the art review. Eng Fract Mech 55:831–857

36. Shifrin E, Ruotolo R (1999) Natural frequencies of a beam with an arbitrary number of cracks. J Sound Vib 222:409–423

37. Gayen D, Tiwari R, Chakraborty D (2019) Static and dynamic analyses of cracked functionally graded structural components: a review. Compos Part B Eng 173:106982

38. Song MT, Gong YH, Yang J, Zhu WD, Kitipornchai S (2019) Free vibration and buckling analyses of edge-cracked functionally graded multilayer graphene nanoplatelet-reinforced composite beams resting on an elastic foundation. J Sound Vib 458:89–108

39. Broek D (2012) Elementary engineering fracture mechanics. Springer Science & Business Media, Berlin

40. Erdogan F, Wu BH (1997) The surface crack problem for a plate with functionally graded properties. ASME J Appl Mech 64(3):449–456

41. Guo LC, Wu LZ, Zeng T (2005) The dynamic response of an edge crack in a functionally graded orthotropic strip. Mech Res Commun 32:385–400

42. Song MT, Chen L, Yang J, Zhu WD, Kitipornchai S (2019) Thermal buckling and postbuckling of edge-cracked functionally graded multilayer graphene nanocomposite beams on an elastic foundation. Int J Mech Sci 161:105040

43. Zhu LF, Ke LL, Xiang Y, Zhu XQ (2020) Free vibration and damage identification of cracked functionally graded plates. Compos Struct 250:112517

44. Yang J, Chen Y (2008) Free vibration and buckling analyses of functionally graded beams with edge cracks. Compos Struct 83:48–60

45. Kitipornchai S, Ke LL, Yang J, Xiang Y (2009) Nonlinear vibration of edge cracked functionally graded Timoshenko beams. J Sound Vib 324:962–982

46. Ke LL, Wang Y, Yang J, Kitipornchai S, Alam F (2012) Nonlinear vibration of edged cracked FGM beams using differential quadrature method. Sci China Phys Mech Astron 55:2114–2121

47. Ke LL, Yang J, Kitipornchai S (2009) Postbuckling analysis of edge cracked functionally graded Timoshenko beams under end shortening. Compos Struct 90:152–160

48. Zhu LF, Ke LL, Xiang Y, Zhu XQ, Wang YS (2020) Vibrational power flow analysis of cracked functionally graded beams. Thin Walled Struct 150:106626

49. Sinha GP, Kumar B (2020) Review on vibration analysis of functionally graded material structural components with cracks. J Vib Eng Technol 9:23–49

50. Suresh S, Mortensen A (1997) Functionally graded metals and metal-ceramic composites: part 2 thermomechanical behaviour. Int Mater Rev 42:85–116

51. Song MT, Gong YH, Yang J, Zhu WD, Kitipornchai S (2020) Nonlinear free vibration of cracked functionally graded graphene platelet-reinforced nanocomposite beams in thermal environments. J Sound Vib 468:115115

52. Rafiee M, Yang J, Kitipornchai S (2013) Large amplitude vibration of carbon nanotube reinforced functionally graded composite beams with piezoelectric layers. Compos Struct 96:716–725

53. Zhang YH, Niu HP, Xie SL, Zhang XN (2008) Numerical and experimental investigation of active vibration control in a cylindrical shell partially covered by a laminated PVDF actuator. Smart Mater Struct 17:035024

54. Selim BA, Zhang LW, Liew KM (2016) Active vibration control of FGM plates with piezoelectric layers based on Reddy's higher-order shear deformation theory. Compos Struct 155:118–134

55. Selim BA, Zhang LW, Liew KM (2017) Active vibration control of CNT-reinforced composite plates with piezoelectric layers based on Reddy's higher-order shear deformation theory. Compos Struct 163:350–364

56. Selim BAMM, Liu Z, Liew KM (2020) Active control of functionally graded carbon nanotube-reinforced composite plates with piezoelectric layers subjected to impact loading. J Vib Control 26:581–598

57. AkhavanAlavi S, Mohammadimehr M, Edjtahed S (2019) Active control of micro Reddy beam integrated with functionally graded nanocomposite sensor and actuator based on linear quadratic regulator method. Eur J Mech A Solids 74:449–461

58. Shokrieh MM, Ghoreishi SM, Esmkhani M (2015) Toughening mechanisms of nano particle-reinforced polymers. In: Toughening mechanisms in composite materials, pp 295–320

59. Liew KM, Yang J, Kitipornchai S (2003) Postbuckling of piezoelectric FGM plates subject to thermo-electro-mechanical loading. Int J Solids Struct 40:3869–3892

60. Wang Q (2002) On buckling of column structures with a pair of piezoelectric layers. Eng Struct 24:199–205

Publisher's Note Springer Nature remains neutral with regard to jurisdictional claims in published maps and institutional affiliations.